AALBORG UNIVERSITY

MASTER'S THESIS

Numerical assessment on pile stability in liquefiable soil

MSc Student
Aske T. MIKKELSEN

Supervisors
Søren D. NIELSEN, Aalborg University
Martin U. ØSTERGAARD, COWI A/S

June 8, 2018

MSc. Structural & Civil Engineering
4th Semester
Thomas Mans vej 23
9220 Aalborg East

Title:
Numerical assessment on pile stability in liquefiable soil

Theme:
Liquefaction, Pile stability
UBC3D-PLM, Plaxis 3D

Project period:
Spring semester 2018
February 1st 2018
to June 8th 2018

Supervisor(s):
Søren D. NIELSEN[1]
Martin U. ØSTERGAARD [2]

Number of pages: 64

Number of pages in appendices: 7

Abstract:

Due to a growing interest in using renewable energy from offshore wind turbines, expanding to regional areas prone to earthquakes can lead to liquefaction problems around the turbine foundation. This report investigates the pile response in liquefiable soil from an earthquake load. The investigation is carried out in PLAXIS3D with the advanced soil model UBC3D-PLM. The soil parameters are calibrated with multistage triaxial test. A post-liquefied analysis is undertaken to establish a relation between the p-y curves and residual shear strength and stiffness in the liquefied soil. The evolution of the excess pore pressure ratio around the pile is assessed along the pile displacement during the dynamic load.

Student:

Aske T. Mikkelsen

The content of the report is freely available, but publication (with source reference) may only take place in agreement with the author.

[1] *Aalborg University*

[2] *COWI A/S*

Preface

This Master's thesis is the final project in the acknowledgement of becoming Msc in Structural and Civil Engineering at Aalborg University, Denmark. The project is carried out from February 1st 2018 to June 8th 2018.

This interest in the theme of the master's thesis, liquefaction and its affect on pile stability for offshore wind turbines, hatched on the preceding semester. Here I had the opportunity to do an in depth collaboration with a company and working on a advanced problem relevant for the industry; Liquefaction around monopiles for offshore wind turbines. The interest, however, did not fade and I therefore used my acquired knowledge on the theory of liquefaction to undertake a numerical approach to assess the liquefaction effects in case studies.

The quality of this master's thesis could not have been greater without the supervision from Søren D. Nielsen and Martin U. Østergaard during the whole project. Their tireless help to guide me in the right direction and extensive interest in the project helped me keep motivated and on point. Their help is greatly appreciated.

Furthermore, a special thank is justified to Daniel D. Cramer, Benjamin Refsgard & Thomas A. Jensen and Alexander Achton-Boel to assist with additional computers in an attempt to ease the demanding and vexatious computational calculations. Finally, a big appreciation for technical discussions to Boris Sørensen and Brian Bjerrum, who have helped me with every little and large problems.

Reading Guide

References to literature is denoted with Harvard notation, i.e the reference have format as Surname,(Year). If more than one citation is made the difference references are distinguished with a ";". The references are collected in a bibliography at the very end of the report in alphabetical order. Labelling of figures and tables are done in accordance to the corresponding chapter for which they are placed. Equations are labelled in the same way with numbering denoting first the chapter and then the order, e.g Eq (1.1) and Eq (2.1) belong to Chapter 1 and 2, respectively.

Throughout the report, units will be given in the SI-format and if nothing else is mentioned compressive stresses and strains are positive to adapt to geotechnical conventions. However, in Chapter 3 the formulas stems from a continuum approach so signs have been changed, where compressive stresses and strains are negative duo to conventions in continuum formulas. The first time a variable is presented in a formula a description of the variable is provided right below the formula.

Contents

Preface v

1 Introduction 1

1.1 Scope of the project 3

2 Literature review 5

2.1 Categorization 5

3 Constitutive soil model UBC3D-PLM 9

3.1 Constitutive modelling in finite element analyses 10

3.1.1 Stiffness parameters and behaviour 10

3.1.2 Plastic response 10

3.1.3 Advanced parameters and behaviour 13

4 Calibration 17

4.1 Data processing 17

4.2 PLAXIS calibration 20

5 Numerical setup 25

5.1 From reality to conceptual model 25

5.2 Geometric dimensions 25

5.3 Boundary conditions 27

5.4 Structure creation 28

5.5 Soil parameters 29

5.6 Mesh generation 29

5.6.1 Convergence analysis 30

5.7 Calculation 31

6 Results 33

6.1 Results for the excess pore pressure ratio 34

6.2 Pile displacement during earthquake load 35

6.3 Post-liquefaction soil strength and stiffness 36

7 Final Remarks 41
7.1 Discussion of results 41
7.1.1 Calibration of the soil model 41
7.1.2 Case results 41
7.1.3 Post-liquefaction soil pressure 42
7.2 Conclusion 44
A Excess Pore Pressure Ratio 1
B Verification of code to establish p-y relation 7

Chapter 1

Introduction

In the last century the use of fossil fuel and the emission of carbon dioxide and methane have been an increasing focus due to the rapid climate changes observed around the world (COP21, 2015). A need for alternatives to fossil fuel is therefore more than ever urgent, and an obvious solution is to utilize more renewable energy. One of the easiest sources of renewable energy is from wind since it is not restricted to geographical location or limited to daytime operation as solar energy for instance is. However, in order to meet the current demands of energy in the world the modern wind turbines need to be more efficient and bigger to able to produce enough energy. A social consequence of bigger wind turbines is an increase in noise and overall aesthetics, so the turbines have to be placed far away from populated areas, for example out in the sea. Constructing out in the sea introduced some new aspects of foundation problems, as loads from waves and ice have to be taken into account in both horizontal and vertical forces, and the soil is often of a more loose and soft character. Shown in Figure 1.1 is a simple schematic drawing of an offshore wind turbine founded on a monopile. The sum of the vertical and horizontal loads are represented in a simplistic manner with arrows. Typically, when designing a monopile, it is modelled as an elastic beam, with either Bernoulli–Euler or Timoshenko beam elements (Kallehave et al., 2015). The lateral bearing component stems for the soils ability to withstand the pressure excited from the wind and waves on the pile. The pile-soil response is then modelled as non-linear springs distributed along the length of the pile. These springs are commonly referred to as *p-y* springs, since they relate the soil resistance acting on the pile p and the lateral displacement y. The stiffness of the springs are highly assosiated with the stiffness of the soil. For sand and clay the p-y formulation is widely established and used for rough design of pile foundation (DNV, 2007). However, the formulations are based on a slender pile with a length of the pile much greater than the diameter (as with e.g. jacket foundations), so caution is to be advised when using these formulations for monopiles, where the diameter is much larger. Nonetheless, the p-y method is still used in the predesign as the calculations are faster compared to more time consuming, but more exact, finite element calculations.

As the demand for more renewable energy increases world wide the interest in establishing offshore wind turbine farms expands to further regions, where the design loads may change. Such a case is around east Asia, where seismic activity from earthquakes is high and very often is a more critical design parameter. Seismicity affects the whole wind turbine in all its components, but in this the focus is on the foundation and soil.

Earthquake excitation

In regions around the Pacific, and especially around the Philippine Sea, large earthquakes are prone to terrorize, see Figure 1.2 , and thus making it difficult to build on soil sensitive to vibrations.

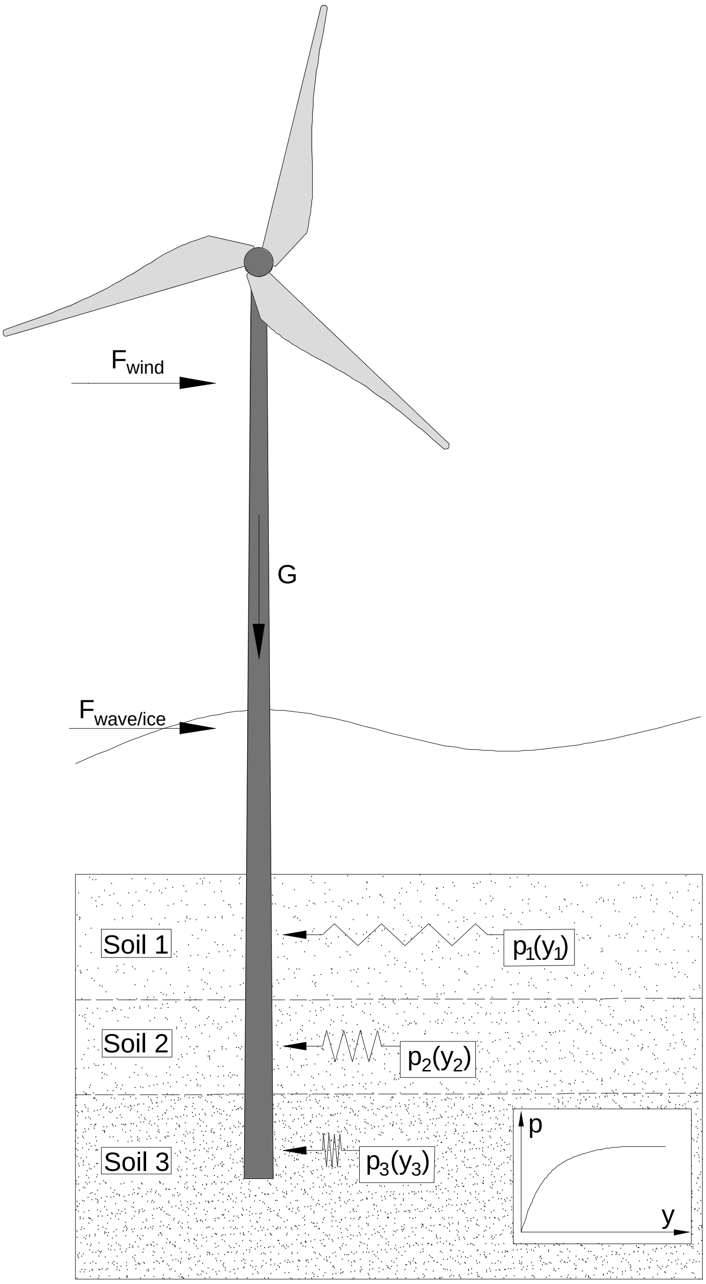

Figure 1.1: *Schematic model of an offshore monopile. $F_{subscript}$ and G are loads. The soil resistance is illustrated by the p(y) springs, which differ in stiffness through the strata.*

Sensitive soil, in this regard, are soil deposits that are in such a state that the excitation from an earthquake severely changes the soil skeleton, and thereby the state, in which the soil is in causing the soil to behave differently prior to the earthquake than after the earthquake. For loose saturated granular material such a dynamic load can lead to *liquefaction*, which is a phenomenon where the effective stress, together with the strength in the soil, drastically decreases or vanishes completely.

Liquefaction happens when the pore pressure in saturated loose soil increases due to the tendency for the soil to densify, but is incapable of because the boundary conditions does not permit the pore water to dissipate and the rate of the dynamic loading is too great. If then a monopile is founded in soil susceptible to liquefaction, engineers have to consider the case of liquefied induced decrease of soil strength and how it effects the pile dimensions and thus the extra financial cost of a

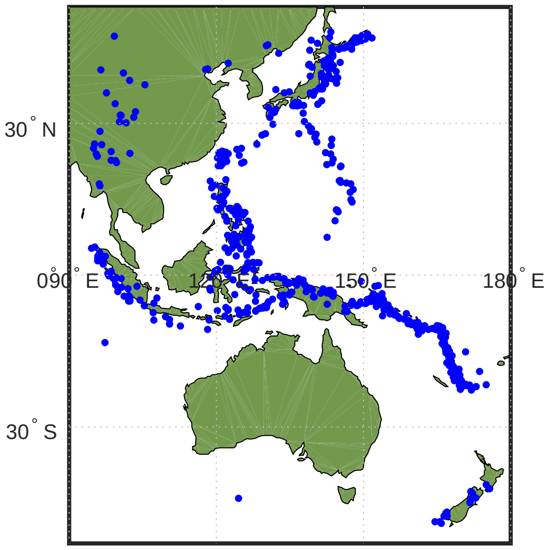

Figure 1.2: *Earthquakes in regions around the Philippine Sea the last 100 years with a moment magnitude of 5 or higher. Data are extracted from* `www.usgs.gov`

evidently bigger monopile.

As of today the standards for the European society offers no specific recommendation for addressing liquefaction deformation, but merely states that for constructions founded in earthquake active regions the susceptibility of liquefaction must be assessed. Eurocode 8 provides some guidelines for qualitatively apprising the susceptibility of liquefaction by utilizing some simple in situ and laboratory tests. Such guidelines include the normalized blow count N_{SPT} from a standard penetration test and the grain size distribution.

Engineeringly, liquefaction can be viewed as merely another state in which the soil can be in with its own constitutive behaviour, in the same way as the differences between sand and clay, (Jefferies and Been, 2015). Compared to the well acknowledge p-y formulations for sand and clay there exist no broadly recognized formulation for liquefied sand, as the current standard is to simply reduced the p-y expression for sand in the pre-liquefaction state by a p-multiplier based on blow counts from SPT, Ashford et al. (2011). This method though erroneously sets the initial stiffness of the liquefied soil too high compared to laboratory test (Lombardi et al., 2014; Rouholamin et al., 2017; Sivathayalan and Yazdi, 2004). Researchers have tried to formulate a p-y expression for liquefied sand based on a curve fit from experimental data (Lombardi et al., 2017; Dash et al., 2017), although its credibility lacks statistical evidence.

1.1 Scope of the project

The main focus of this report is thus not to describe and analyze the phenomenon *liquefaction* in length, but to apply theoretical and experimental knowledge in practical applications. Due to expanding of offshore wind turbines to areas with high earthquake activity, the need to more qualitatively address the consequences of liquefaction is becoming more prudent in order to optimize the construction phase. This is done by looking into the modelling of liquefaction through a constitutive soil model within a numerical framework. The perspective of the project will be in form of a case study for a monopile for offshore wind turbines, where the goal of interest will be how the appearance of liquefaction influences the soil strength and stiffness of the soil and displacement of the monopile.

Typical lateral loads on an offshore monopile consist of wind, wave and ice bricks floating on top of the ocean hitting the structure. The complexity in determining the different load combinations of said loads and assessing the consequences is out of the scope of the project. Although wind and waves can change rapidly over a short time period, they are regarded as a static combined lateral load in this report. This is mainly done in order to simplify the calculations and to shift the focus away from the dynamics of these loads and onto the dynamic loads from earthquakes, as this excitation much more often leads to a critical level of excess pore pressure.

The calculations are carried out in PLAXIS with its advanced soil model called *UBC3D-PLM*, which is a more generalized version of the previous soil model *UBCSAND*. The input parameters in soil model will be calibrated with cyclic triaxial data to give more accurate results. The soil model is validated in its ability to model liquefaction by generation of excess pore pressure and reducing the effective stresses. A static analysis is carried out at the end of the dynamic calculation in an attempt to establish an alternative relation of the p-y expression for post-liquefied sand.

A more detailed description of liquefaction than given in this chapter will not be given further in the report, but an understanding based on the description in e.g (Kramer, 1996) will be sufficient. However, important parameters in the aspect of liquefaction will briefly be defined when they appear in the report to minimize misunderstanding when definitions are unclear or not well-known.

Chapter 2

Literature review

2.1 Categorization

Before initiating the actual analyses it is desirable to commence a literature review of the current knowledge and investigations published in the aspect of the scope of the project. The purpose of this review is twofolded:

1. Highlight previous studies which have investigated parts similar to the scope of the project. This is done to make a base of reference and making sure there is consensus across the research.
2. Highlight weak points in the current knowledge. Weak points are areas where there are no or very little research done and by that premise endorse the intent of the project. This is an arduous task since it basically requires to find something that is not there.

The articles looked at are systematic arranged in categories depending on their focus related to the project. In the succeeding subsections the categories are looked at one by one with the a short presentation of relevant articles for that current category.

Category A

The articles in this category establishes a reference of the basic mechanics involved in cyclic shearing of undrained granular soil and the post-liquefied behaviour in undrained monotonic shearing.

Lombardi et al. (2014), Lombardi et al. (2017) Rouholamin et al. (2017), Dash et al. (2017), Sivathayalan and Yazdi (2004): These articles focus on the relation between soil conditions and stress states with the onset of liquefaction and post-liquefaction behaviour of different types of granular material. The results all show similar trend with low relative density as an important soil characteristic in the onset of liquefaction and the post-liquefaction behaviour. The results stem from laboratory test with a cyclic phase, either in triaxial apparatus or as a cyclic direct simple shear test. The conclusion on the post-liquefied soil behavior is coherent, where the soil hardens as strains increase and has a concave curve.

Category B

In close relation to the previous category these articles look at site investigation and large scale tests, where the soil-structure interaction is taken into accounts.

Byrne et al. (2000); Butterfield and Davis (2004); Chang and Hutchinson (2013); Janalizadeh and Zahmatkesh (2015); Ghorbani (2017); Bao et al. (2017) These articles compare the examined behaviour from laboratory test with field test and site investigation of observed liquefaction in nature. The CANLEX experiment (Byrne et al., 2000) was a huge collaborate field investigation aimed at statically trigger liquefaction in a loose foundation layer underlying a clay embankment. The test results were compared with the finite element simulation using the constitutive soil model UBCSAND. The comparison showed good agreement between the field results and the soil model UBCSAND.

Butterfield and Davis (2004) focuses on downhole recordings of ground accelerations to validate a proposed shear strain threshold hypothesis, at which the times the strains surpass a certain threshold matches the build up of excess pore pressure. The comparison were done for four different earthquakes, where only one (the Superstition Hills earthquake) showed discrepancy between the time of threshold exceedence and rise in pore pressure.

In **Chang and Hutchinson (2013); Janalizadeh and Zahmatkesh (2015)** large scale test on a single pile surronded by loose saturated soil is subjected to sequential dynamic shaking. The tests aimed at establishing insigt in the lateral resistance, 'p-y' resistance, in liquefied soil. Different loading patterns were conducted and the overall trend for p-y curves showed an S-shape curvature (Chang and Hutchinson, 2013), with low stiffness at small displacements and stiffness at large displacements. Janalizadeh and Zahmatkesh (2015) mentions as an addition that a maximum bending moment occurs in the interface between the liquefiable soil and the non-liquefiable soil

In **Luque and Bray (2017)** the Canterbury earthquake in Australia is replicated by modelling the nonlinear dynamic soil-structure interaction and compares the results with the observed response of the ground and the structure during the earthquake. The article concludes that the deformation failure were do to loss of bearing capacity in the foundation as the excess pore pressure developed during the earthquake.

This article by **Ghorbani (2017)** investigates the dynamic response of pile foundation and assess the accuracy of 2D numerical simulations for 3D effects such as shadow and neighboring effects in pile groups. The results are compared with measured values from a shaking table test. The investigation is done using a Finite Difference Method in FLAC2D with the constitutive model *Finn*. The analysis approach was constructed of three phases. The simulation indicate a residual bending moment at the end of the shaking, although with a tendency to under-predict the maximum bending moment during the dynamic loading.

The baseline of **Bao et al. (2017)** is an analysis of the seismic behavior subway tunnel founded in liquefiable ground. A key focus in the article is to address the uplift tendency of the tunnel when the surrounding soil starts to liquefy. The simulation of liquefaction detects a significant lower excess pore water pressure near the structure compared to that in free field at same depth.

Category C

In a more numerical related connection to the scope of this report these article utilize either the soil model UBC3D-PLM or its predecessor UBCSAND.

Wobbes et al. (2017); Daftari and Kudla (2014) focus on simulation of liquefaction with the soil model UBC3D-PLM (Wobbes et al., 2017) and the former UBCSAND (Daftari and Kudla, 2014). The simulations are solely done for evaluating the build up of excess pore pressure and degradation of effective stresses. A comparison is done with a shaking table test and the Superstition Hill Earthquake. The results show an expected development of excess pore pressure with a top-down trend for the numerical simulation of the excess pore pressure, see Figure 2.1 . A comparison with the measurement from the shaking table test and the recordings from the earthquake likewise indicate good agreement in the identification of liquefaction.

Daoud et al. (2018) aims to develop a dynamic numerical model in order to assess the liquefaction potential of a shipped ore. It initiates the research by a calibration of the soil model UBCSAND with a cyclic triaxial test. The article addresses a few limitations of the soil model which includes the irregular evolutions of axial strain and effective stresses when the soil approaches the liquefied state. The article concludes that the UBCSAND model fairly accurately predicts the experimental results from a cyclic triaxial test with emphasize on the evolution of the excess pore pressure.

Overall there is consensus across the articles about the behaviour and soil mechanics involved with cyclic shearing, onset of liquefaction and post-liquefaction behaviour. The different constitutive soil models utilized to imitate the build up of excess pore pressure also fairly accurately resembles that of experimental test. The general trend seen in both experiments and numerical work is top-down trend of liquefaction.

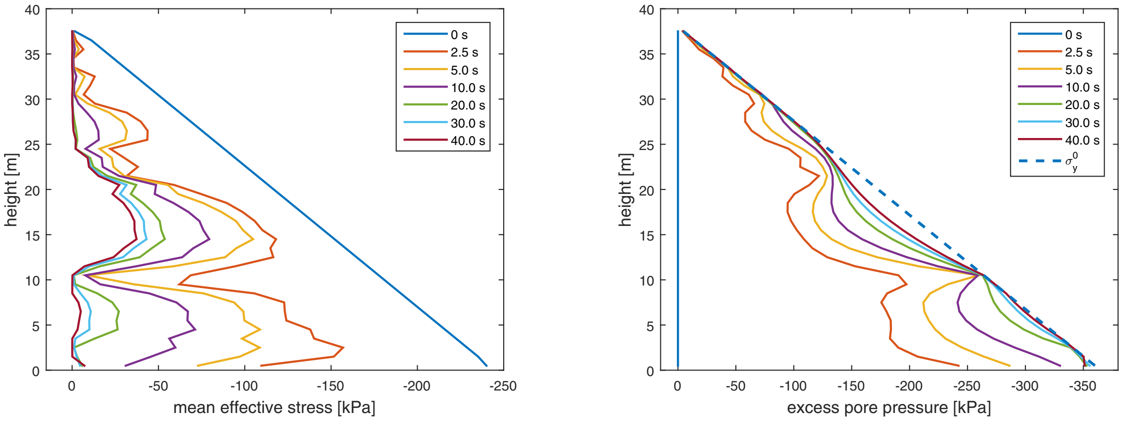

Figure 2.1: *Left: Degradation of the mean effective stress along the soil column at different time steps. Right: Build up of excess pore pressure along the soil column at different time steps.Wobbes et al. (2017)*

Chapter 3

Constitutive soil model UBC3D-PLM

Under cyclic loading, e.g. during an earthquake, dry granular soil will compact and densify. If the soil is saturated, and the load rate is fast compared to hydraulic conductivity and seepage, the soil cannot densify as there is no longer air in the pores to allow rearranging of the soil particles, but water instead. This is an undrained behaviour. However, the saturated soil will still try to densify causing an increase in the pore pressure on the particles. This excess pore pressure will result in a further decrease of the effective stress besides the hydrostatic pressure. Eventually, the excess pore pressure on the grains equalize the effective contact pressure on the grains themselves resulting in a fluid like behaviour. When this happens, liquefaction has occurred, c.f. R.B.J Brinkgreve (2017).

This relation between pore pressure and contact pressure can be explained from the well-known Coloumb's formula (3.1) and Terzaghi's formula (3.2)

$$\tau = \sigma'_{v0} \tan\phi \tag{3.1}$$

$$\sigma'_{v0} = \sigma_{v0} - p_w \tag{3.2}$$

τ	Shear resistance
σ'_{v0}	Initial effective stress
σ_{v0}	Total stress
p_w	Hydrostatic pore pressure
ϕ	Friction angle

When the excess pore pressure develops Terzaghi's formula is rewritten into

$$\sigma'_{v0} = \sigma_{v0} - (p_w + \Delta p_w) \tag{3.3}$$

Δp_w	Excess pore pressure

which means that when Δp_w increases, σ' decreases and leading back to Eq. (3.1) the shear resistance drops.

The predisposing factors for Δp_w to develop during an earthquake depend on different geological factors of the soil, such as the particle size, shape and gradation, but also the magnitude and duration of the earthquake and the drainage conditions in the surrounding soil. Different methods to assess the susceptibility of liquefaction can be used from semi-empirical field investigations and laboratory tests to dynamic finite element analyses.

3.1 Constitutive modelling in finite element analyses

To trace the onset of liquefaction in a finite element investigation, the material model utilized needs to capture the build up of excess pore pressure due to volumetric strains. A suggestion of such a material model is the UBC3D-PLM implemented in PLAXIS3D that is especially developed for liquefaction assessment.

The abbreviation of the model stands for **U**niversity of **B**ritish **C**olumbia in **3 D**imensions, **P**LAXIS **L**iquefaction **M**odel. It is a generalized model of the UBCSAND, which was also produced at the University of British Columbia. As the name implies, the new version is able to address the soil behaviour in all three dimensions, where its predecessor is only useful in two dimensions.

The UBC3D-PLM soil model is a non-linear constitutive model that is developed on the basis of the Mohr-Coloumb yield criterion, Drucker-Prager for the non-associated plastic potential function and Rowe's stress dilatancy. In a total, the UBC3D-PLM model depends on 11 special parameters besides the usual material parameters such as the specific weight. The 11 parameters can be divided into six parameters for the stiffness, three advanced parameters and two for strength (peak internal friction angle and friction angle at constant volume).

3.1.1 Stiffness parameters and behaviour

The six parameters controlling the stiffness are

k_B^e	Elastic bulk modulus factor	[-]
k_G^e	Elastic shear modulus factor	[-]
me	Elastic bulk modulus index	[-]
ne	Elastic shear modulus index	[-]
k_G^p	Plastic shear modulus factor	[-]
np	Plastic shear modulus index	[-]

Elastic response

The elastic behaviour of the model is controlled by the *elastic bulk modulus K* and the *elastic shear modulus G* defined as

$$K = k_B^e p_{ref} \left(\frac{\sigma}{p_{ref}} \right)^{me} \tag{3.4}$$

$$G = k_G^e p_{ref} \left(\frac{\sigma}{p_{ref}} \right)^{ne} \tag{3.5}$$

p_{ref}	Reference pressure (often set as the atmospheric pressure), [kPa]
σ	Mean stress, [kPa]

As it can be seen the elastic stiffness are stress dependent. The exponents, *me* and *ne*, control the rate at which the stiffness changes due to changes in stress.

3.1.2 Plastic response

As the stresses increases the stress state reaches the yield surface defined by Mohr-Coloumb yield criterion;

$$f = 0 = \frac{\sigma_1 - \sigma_3}{2} - \left(\frac{\sigma_1 + \sigma_3}{2} + c \ \cot \phi_p \right) \sin \phi_m \tag{3.6}$$

σ_1	Maximum principal stress, [kPa]
σ_3	Minimum principal stress, [kPa]
c	Cohesion, [kPa]
ϕ_p	Peak friction angle, [°]
ϕ_m	Mobilised friction angle, [°]

By rearranging (3.6) and setting the cohesion to zero the sine of the mobilised friction angle can be expressed as

$$0 = \frac{\sigma_1 - \sigma_3}{2} - \left(\frac{\sigma_1 + \sigma_3}{2}\right)\sin\phi_m = \tau_m - \sigma'_m \sin\phi_m \tag{3.7}$$

$$\sin\phi_m = \frac{\tau_m}{\sigma'_m} = Stressratio \tag{3.8}$$

τ_m	Mobilised shear stress, [kPa]
σ'_m	Mobilised mean effective stress

In a τ, σ'-plot the yield surface is depicted as a straight line rooting from origo, see Figure 3.1 . The current stress state, point A, controls the yield surface for first time shear loading. Once the shear stress increases, the stress ratio increases as well causing the stress state to move from point A to point B. The yield surface is now expanded to point B. This increase in stress state from A to B and movement of the yield surface results in plastic strains with both plastic shear strains and plastic volumetric strains.

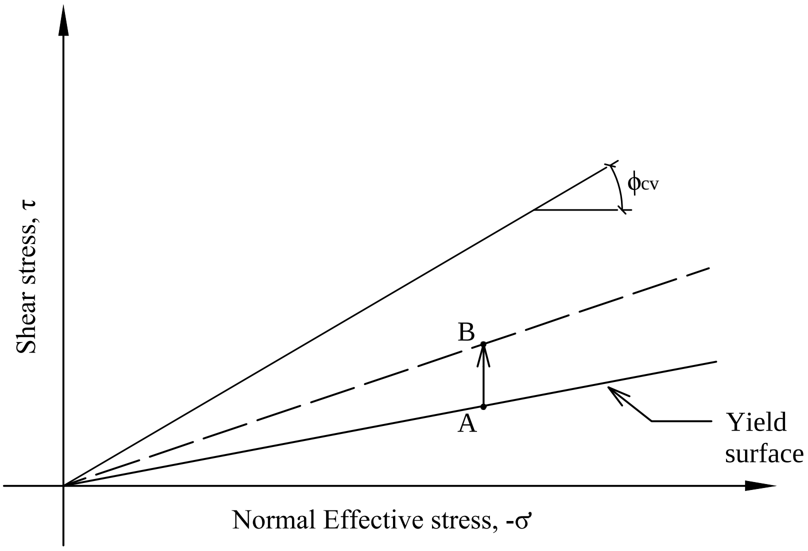

Figure 3.1: *Yield surface.*

Plastic shear strain

The increment of plastic shear strains depend on the changes in the mobilised friction angle and can be defined through the hardening rule, c.f Tsegaye (2010). It is schematically shown in Figure 3.2 as a hyperbolic relation between the developed stress ratio and the plastic shear strain. This relation can be expressed as

$$d\gamma^p = \frac{1}{G^p} d\sin\phi_m \tag{3.9}$$

γ^p	Plastic shear strain
G^p	Plastic shear modulus

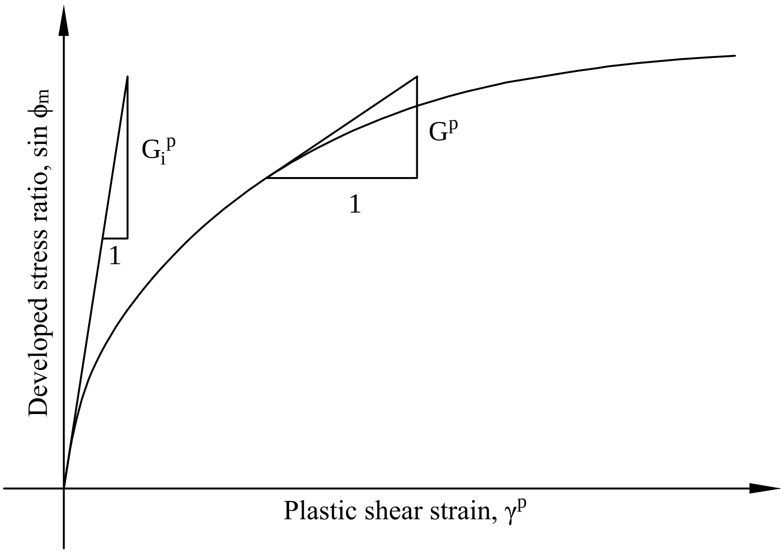

Figure 3.2: *Hardening rule.*

The plastic shear modulus is given by

$$G^p = \frac{G_i^p}{\sigma'_m}\left(1 - \frac{\sin\phi_m}{\sin\phi_p}R_f\right)^2 \tag{3.10}$$

$$G_i^p = k_G^p\left(\frac{\sigma'_m}{p_{ref}}\right)^{np} p_{ref} \tag{3.11}$$

G_i^p	Initial plastic shear modulus (at low stress ratio)
R_f	Failure ratio. Advanced user input parameter and generally varies between 0.5 and 1 and decreases with increasing relative density

The hardening rule utilized in UBC3D-PLM is generally rewritten as, c.f Petalas and Galavi (2013):

$$d\sin\phi_m = 1.5k_G^p\left(\frac{\sigma}{p_{ref}}\right)^{np}\frac{p_{ref}}{\sigma'_m}\left(1 - \frac{\sin\phi_m}{\sin\phi_p}R_f\right)^2 d\lambda \tag{3.12}$$

$d\lambda$	Plastic strain increment multiplier

Plastic potential function

The plastic potential function gives the direction of the plastic strains, and from the potential function the flow rule is established. In UBC3D-PLM the Drucker-Prager plastic potential function is used to define a non-associated flow rule. Softnening problems, as with liquefaction deformations, require non-associated flow rule.

The plastic potential function used in UBC3D-PLM is given as

$$g = q - \frac{6\sin\psi_m}{3-\sin\psi_m}(p+\cot\phi_p) \tag{3.13}$$

$$q = \sqrt{\frac{1}{2}\left[(\sigma_1-\sigma_2)^2+(\sigma_2-\sigma_3)^2(\sigma_1-\sigma_3)^2\right]} \tag{3.14}$$

$$p = -\frac{\sigma_1+\sigma_2+\sigma_3}{3} \tag{3.15}$$

g	Plastic potential function
q	Deviatoric stress
p	Hydrostatic pressure
ψ_m	Mobilised dilatancy angle

Plastic volumetric strain

The associated plastic volumetric strain to plastic shear strain is defined based on Rowe's stress dilatancy. The relation between the increment of plastic volumetric strain to the increment of plastic shear strain is given as

$$d\varepsilon_v^p = \sin\psi_m d\gamma^p \tag{3.16}$$

$$\sin\psi_m = \sin\phi_m - \sin\phi_{cv} \tag{3.17}$$

$d\varepsilon_v^p$	Incremental plastic volumetric strain
ϕ_{cv}	Constant volume friction angle

The flow rule is based on three observations, c.f Petalas and Galavi (2013),:

1. There is a unique stress ratio at which plastic shear strain does not produce plastic volumetric strain. This stress ratio is defined for $\sin\phi_m = \sin\phi_{cv}$

2. When $\sin\phi_m < \sin\phi_{cv}$ contractive behaviour occurs.
   When $\sin\phi_m > \sin\phi_{cv}$ dilative behaviour occurs.

3. The amount of contraction or dilation depends on the difference between the current stress ratio and the stress ratio at $\sin\phi_{cv}$

The flow rule is illustrated in Figure 3.3 . The black arrows denote the direction of the plastic strains, where the arrow in the middle is the first observation. The two colored regions illustrate the second observation. Above the plot is a small diagram of an arbitrary arrow with visualizing of Eq. (3.16).

3.1.3 Advanced parameters and behaviour

The three advanced parameters are

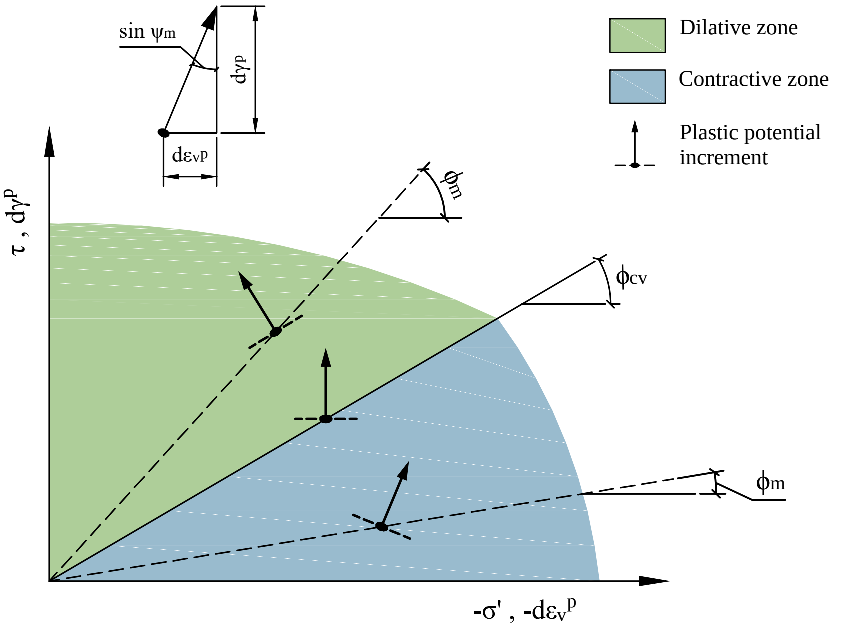

Figure 3.3: *Illustration of flow rule used in UBC3D-PLM.*

f_{dens}	Multiplier to adjust the densification rule	[-]
f_{Epost}	Fitting parameter to adjust post-liquefaction behaviour	[-]
R_f	Failure ratio	[-]

During unloading and reloading the soil model predicts either elastic or plastic behaviour based on a simple unloading-reloading criterion;

$$\sin\phi_m^e < \sin\phi_m^0 \qquad \text{Unloading. Elastic behaviour} \tag{3.18}$$

$$\sin\phi_m^e > \sin\phi_m^0 \qquad \text{Loading or reloading. Plastic behaviour} \tag{3.19}$$

$\sin\phi_m^e$	Mobilised friction angle from current stresses
$\sin\phi_m^0$	Mobilised friction angle from previous stress state

An important feature in the UBC3D-PLM soil model is a densification rule introduced to more accurately predict the evolution of excess pore pressure, Petalas and Galavi (2013). A secondary yield surface is introduced for the secondary loading (not to be confused with the second load cycle), which enables a more smooth transition into liquefaction. The secondary yield surface produces less plastic strain compared to the primary (or dominant) yield surface. Primary loading is when the yield surface expands towards the peak stress state. When the stress reload again after unloading it is secondary loading until the secondary yield surface coincides with the primary yield surface. Further increas in stress will expand the primary yield surface and primary yielding is then present. This is the case later explained in Figure 3.4 .

For the primary yield surface an isotropic hardening rule is used, c.f. Eq. (3.12), whereas for the secondary yield surface a kinematic hardening rule is used. The plastic shear modulus factor k_G^p used in the primary yield surface is identical with the user defined one in Eq. (3.12). For the secondary yield surface k_G^p is altered by taking into account the number of cycles during the loading process in order to capture the effect of soil densification. The number of cycles is defined by the unloading-reloading criterion. The altered k_G^p for the secondary yield surface is formulated as

$$k_{G,sec}^p = k_G^p\left(4+\frac{n_{rev}}{2}\right)\cdot hard\cdot fac_{hard} \tag{3.20}$$

$k_{G,sec}^p$	Plastic shear modulus factor for the secondary yield surface
n_{rev}	Number of shear stress reversals
$hard$	Factor correcting for loose soils and varies between 0.5 and 1
fac_{hard}	User input multiplier to adjust the densification rule

The densification rule and the secondary yield surface are illustrated in Figure 3.4 . In case a) primary loading occurs in the first half load cycle starting from from $q = 0$ and some arbitrary mean effective stress *p'*. Since it is primary loading the initial input parameter k_G^p is used and both the primary and secondary yield surface expand until a maximum stress state.

In case b) elastic unloading is happening and the secondary yield surface moves down until it reaches the isotropic axis. Half a load cycle has now passed. As isotropic hardening is used for the primary loading the primary yield surface stays at the maximum stress state reached so far in the loading progress.

In case c) secondary loading occurs and the secondary yield surface is again dragged upwards.

In case d) elastic unloading is again happening from the maximum stress state down to the isotropic axis. A full load cycle has now passed, and the densification rule is activated ($n_{rev} = 1$).

In case e) secondary loading occurs with the secondary yield surface expanding until it reaches the maximum stress state of the primary yield surface. The stress state continues further and primary loading is predicted until a new maximum stress state. The primary yield surface is now dragged to the new maximum stress state.

In case f) when the primary yield surface touches the peak stress state (indicated with a red line) the secondary yield surface is deactivated.

Post-liquefaction rule

One drawback during modelling of cyclic liquefaction in sand is the locking of volumetric strains. When the stress state reaches the peak stress, defined by the peak friction angle, the change in volumetric strains becomes constant. $\sin\phi_m$ in Eq. (3.17) becomes $\sin\phi_p$ and stays constant while $\sin\phi_{cv}$ is also a constant. It means that the stiffness degradation due to post-liquefaction behaviour cannot be modelled. However, this limitation is overcome by introducing a dilation factor which gradually decreases the plastic shear modulus as function of the generated plastic deviatoric strain during dilation, Petalas and Galavi (2013). The plastic shear modulus degradation is computed as

$$k_{G,post-liq}^p = k_G^p e^{E_{dil}} \tag{3.21}$$

$$E_{dil} = min(110\varepsilon_{dil}, fac_{post}) \tag{3.22}$$

$k_{G,post-liq}^p$	Degraded plastic shear modulus after liquefaction
E_{dil}	Dilation factor
ε_{dil}	Accumulation of the plastic deviatoric strains generated during dilation
fac_{post}	User input parameter that limits the expontial multiplier of the dilation factor.

The failure ratio R_f is already mentioned in Section 3.1.2, however it is denoted as an advanced parameter in PLAXIS3D. The failure ratio is defined as the ratio between the stress ratio at failure and the asymptote for the hyperbolic curve in Figure 3.5 The failure ratio is formulated as

$$R_f = \frac{\sin\phi_{m,ult}}{\sin\phi_{m,f}} \tag{3.23}$$

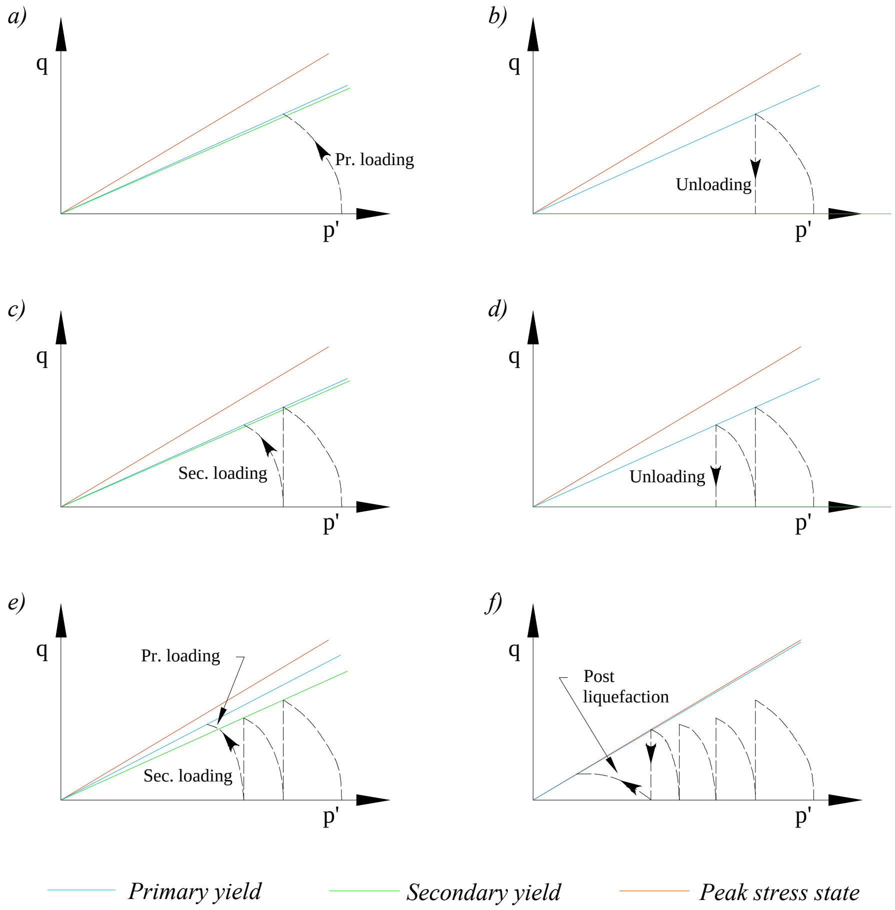
a)
q
p'
Pr. loading
b)
q
p'
Unloading
c)
q
p'
Sec. loading
d)
q
p'
Unloading
e)
q
p'
Pr. loading
Sec. loading
f)
q
p'
Post
liquefaction
Primary yield
Secondary yield
Peak stress state

Figure 3.4: *Introduction of the two yield surfaces and the soil densification.*

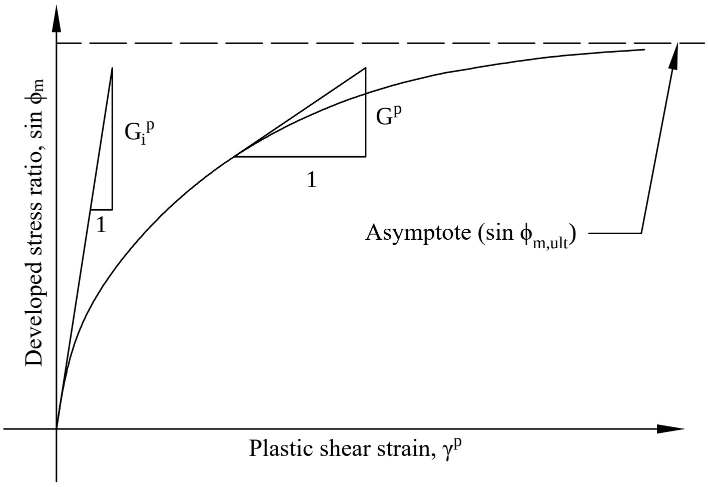
Developed stress ratio, sin ϕm
G_i^p
1
G^p
1
Asymptote (sin ϕm,ult)
Plastic shear strain, γ^p

Figure 3.5: *Asymptote for the ultimate stress ratio.*

Chapter 4

Calibration

4.1 Data processing

The data used for calibrating the soil model UBC3D-PLM is provided by Rouholamin et al. (2017). The data is measurements from a cyclic triaxial test. The test is conducted as a multistage tests with a consolidation stage, followed by a stress controlled cyclic stage and subsequently a post-liquefaction stage of strain controlled monotonic loading. In Figure 4.1 the loading scheme presented in Rouholamin et al. (2017) is illustrated with color indication corresponding to the three stages just mentioned.

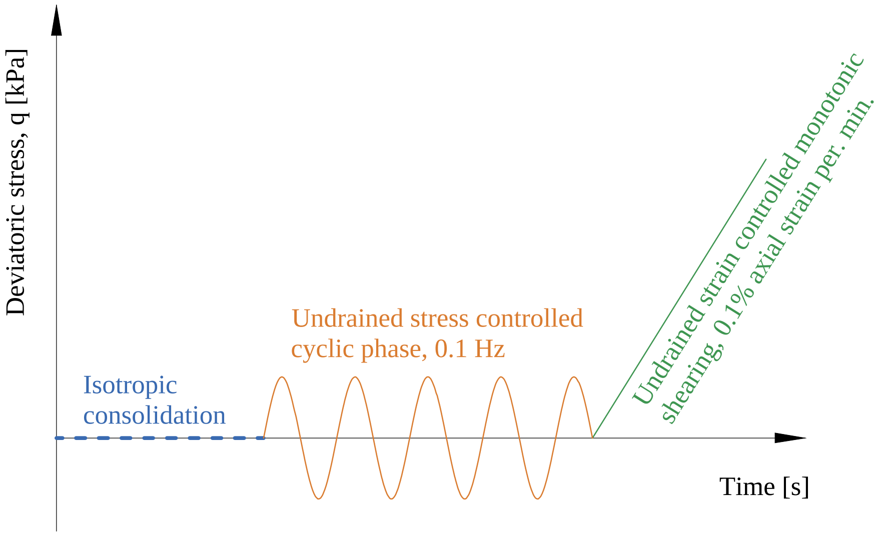
Deviatoric stress, q [kPa]
Isotropic consolidation
Undrained stress controlled cyclic phase, 0.1 Hz
Undrained strain controlled monotonic shearing, 0.1% axial strain per. min.
Time [s]

Figure 4.1: *Loading scheme for multistage cyclic triaxial as described in Rouholamin et al. (2017).*

A first analysis of the test is to plot the deviatoric stress and localize the stage transformations according to the loading scheme. This plot is seen in Figure 4.2 A).

Each stage is plottet with the same color in Figures 4.1 and 4.2 A). The three stages are clearly distinguished between each other, but a quick comparison between the plot and the loading scheme reveals a discrepancy in the consolidation stage. In the loading scheme, and described in Rouholamin et al. (2017), the tests were conducted with an isotropic consolidation ending with a deviatoric stress equal to zero, but as clearly depict in the plot the first stage ends with a deviatoric stress of $q = -13\,\text{kPa}$, hence the first stage more resembles an anisotropic consolidation. However, further use of the data will still assume an isotropic consolidation as the whole consolidation stage is of less importance for the scope of the project. Therefore, the denouement of the consolidation

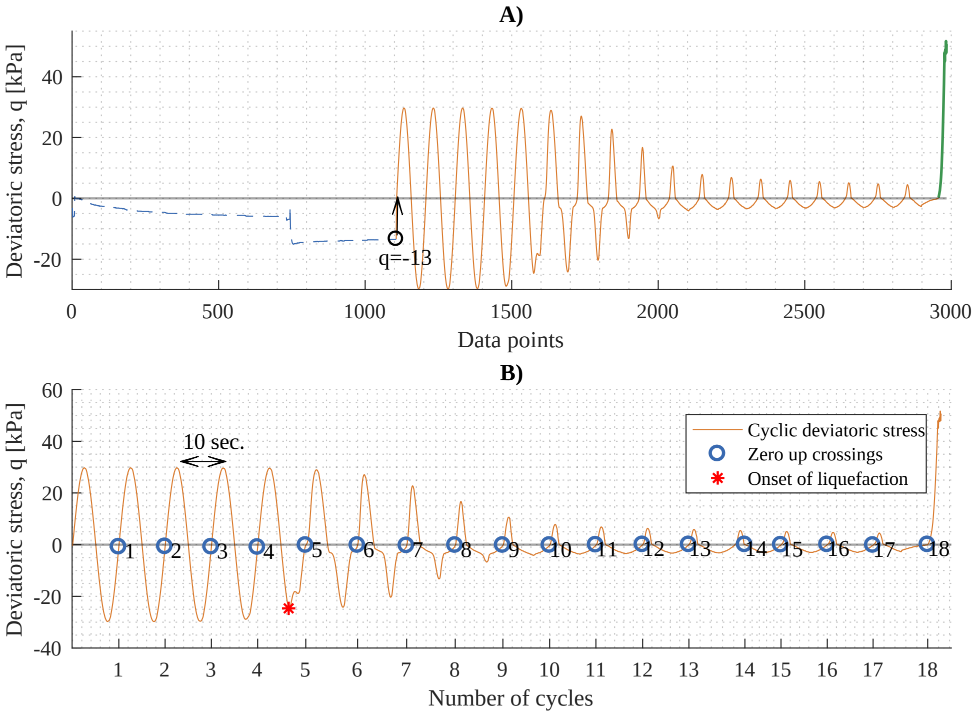

Figure 4.2: *Development of the deviatoric stress and localization of stage transformation for test-1. The upward arrow indicates the assumed ending of the consolidation phase as described in Rouholamin et al. (2017).*

stage is "stretched" to the stress state of zero deviatoric stress (indicated with a black upward arrow).

The interesting part of the loading scheme is the second stage with the cyclic loading phase (marked with an orange color) since it is in this phase the build up of excess pore pressure is happening and hence the part that is calibrated with in PLAXIS. This stage is further analyzed in Figure 4.2 B) with the denotation of the cycles by an zero up-crossing. The cyclic frequency is 0.1 Hz, or a period of 10 s, and with an amplitude of 30 kPa. During the fourth cycle the cyclic stress starts to drift, which is seen by a higher minimum value of the deviatoric stress. Liquefaction is therefore said to initiate in the fourth cycle and this initiation is marked by a red star in the plot. This red star can be traced throughout the subsequent figures to ease the connection between the plots.

The onset of liquefaction is further illustrated in Figure 4.3 A) where the complete stress path is showing. Here the inauguration of liquefaction is again shown with a red star and the characteristic butterfly shape around a zero mean effective stress. As the start of the cyclic phase is assumed to start at a deviatoric stress of $q = 0\,\text{kPa}$ the initial mean effective stress is $p' = 101\,\text{kPa}$, which later will be used for calculating the excess pore pressure ratio.

In Figure 4.3 B) the total pore pressure evolution is illustrated with the three stages marked with color indication. Again, the onset of liquefaction is marked with a red star. The consolidation stage shows a steady linear increase of pore pressure, where the excess pore pressure is the additional increase in pressure happening in the cyclic stage after consolidation. The excess pore pressure is plottet in Figure 4.4 A). In plot B) the ratio between the excess pore pressure and the initial stress is plotted. Here the ratio stabilizes around $r_u = 1$, which means the pore pressure acting one the particle is equal to the effective stresses on the particles.

In Figure 4.5 A) the axial strain development is shown which clearly indicate a stagnation in the first few cycles, but after the initiation of liquefaction the strains rapidly increase. In Figure 4.5

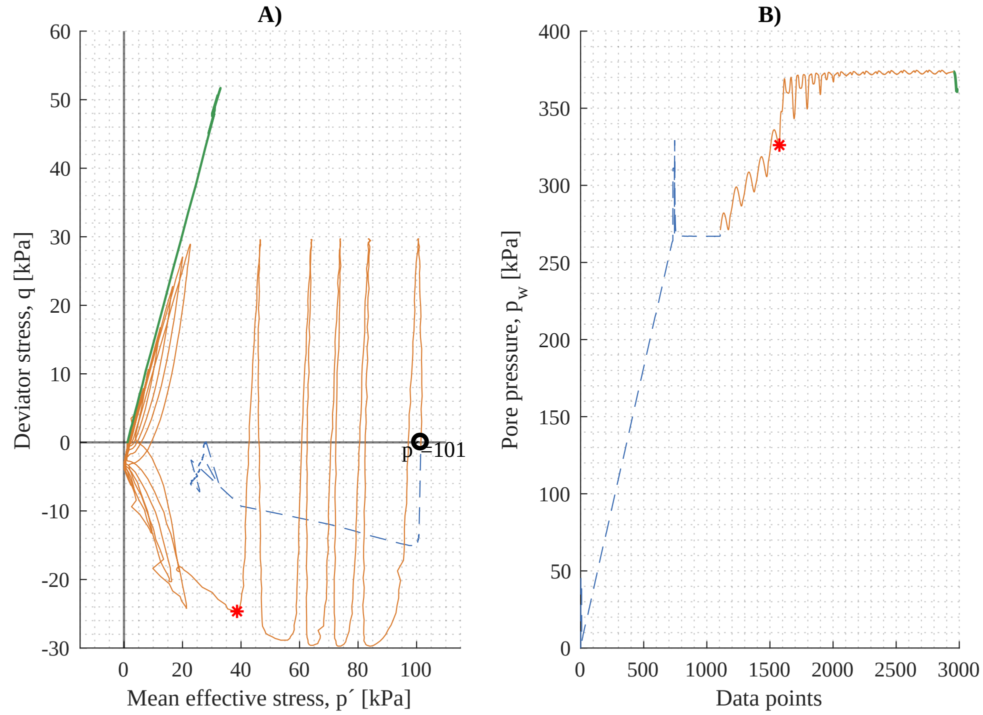

Figure 4.3: *Stress path and pore pressure.*

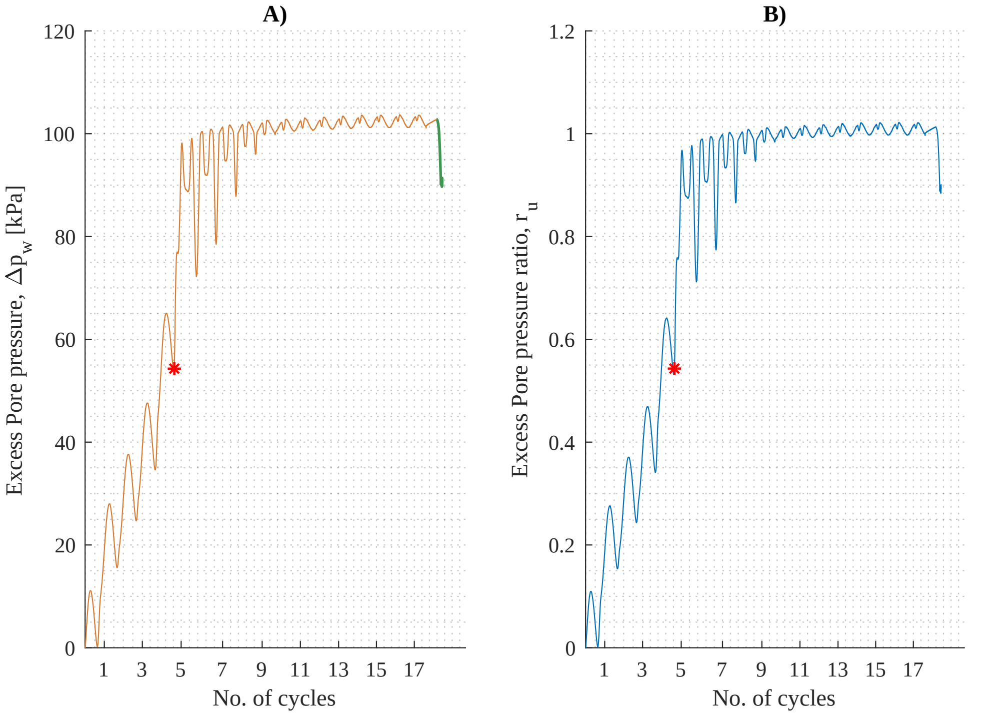

Figure 4.4: *Excess pore pressure Δp_w and excess pore pressure ratio r_u.*

B) the axial strains are illustrated as a function of the number of cycles and it is more clearly seen here how the strains rapidly develop with the onset of liquefaction.

The six plots in Figure 4.3 , Figure 4.4 and Figure 4.5 all show consensus regarding the onset

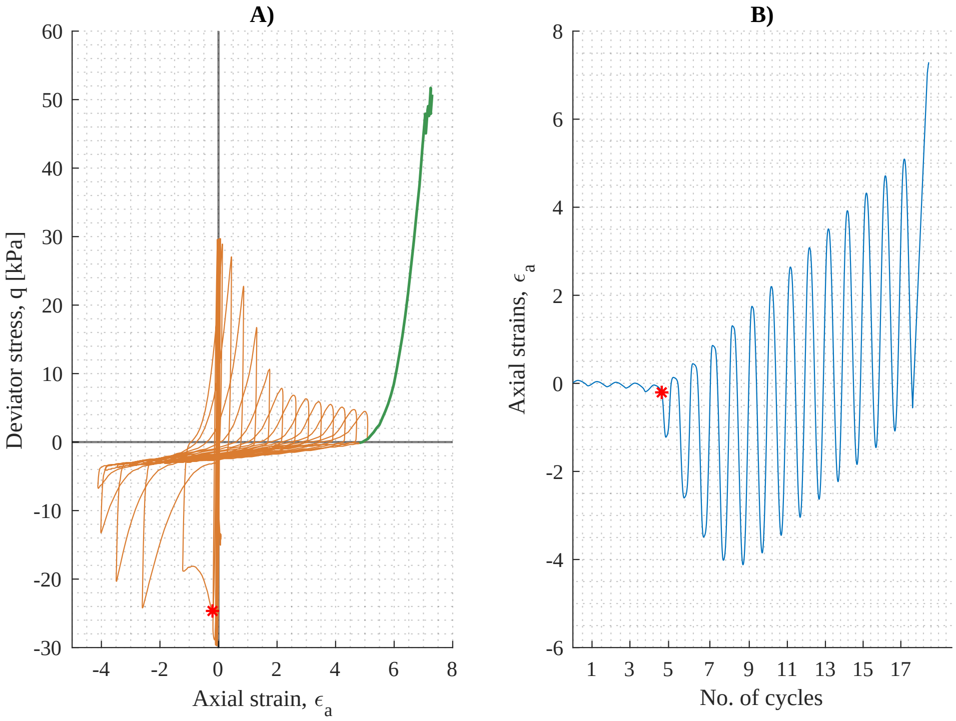

Figure 4.5: *Development of axial strains.*

of liquefaction as the effective stresses reach approximately zero at the same time the excess pore pressure stabilizes around a steady value and the axial strain promptly begins to escalate. These plots, and especially the development of the excess pore pressure, is then further used in calibrating the soil model UBC3D-PLM in PLAXIS 3D.

4.2 PLAXIS calibration

The calibration of the soil model UBC3D-PLM from the laboratory test described in the previous section is done in PLAXIS 3D in the in-build function *SoilTest*. Here it is possible to replicate different types of laboratory test such as conventional monotonic triaxial test, direct simple shear test, consolidation test and more user-defined tests. Since the laboratory test is a cyclic triaxial compression and extension test the calibration is done as a *general soil test*, where the stress state together with the duration for each increment of stress is defined. These durations and stress states are depicted from Figure 4.6 , where the cyclic stage is again plotted, but instead of the deviatoric stress it is only the axial σ_{yy}-stresses. In the figure the first three phases are marked with different colors. A schematic overview of all the phases from Figure 4.6 with stress increments and duration can be seen in Table 4.1 . The table is read in the following way:

$$\sigma_{yy,i+1} = (\sigma_{yy} + Stress\ inc.)_i \qquad \text{where} \quad i = [1:36]$$

The cyclic phase consists of a total of 37 phases that all need to be defined in PLAXIS to replicate the whole cyclic stage from the laboratory test. A screen shot of the setup of the *general test* with the first three phases together with output plots are shown in Figure 4.7 .

The plots used for calibration are "Plot 2" and "Plot 4", and in Table 4.2 the effects of the stiffness parameters in the soil model on the plots are described. The labels in Figure 4.8 help with identifying in what areas of the soil behaviour the parameters influence, as they are is described in the table.

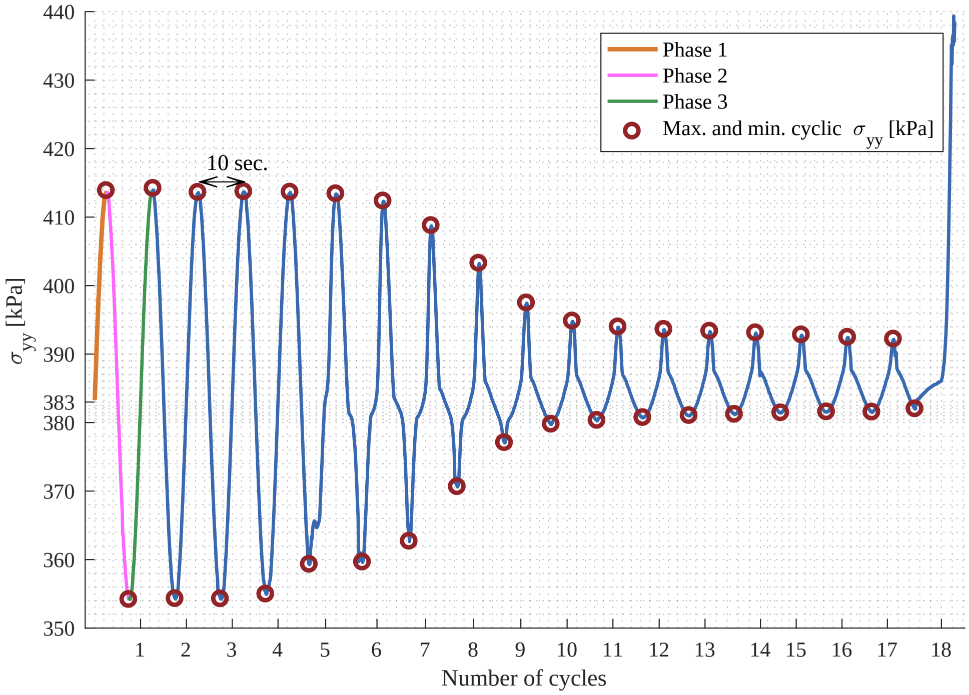

Figure 4.6: *Phase division used for calibrating cyclic triaxial test in PLAXIS3D.*

Table 4.1: *Phase division for calibration in PLAXIS.*

Phase	σ_{yy} [kPa]	Duration [s]	Stress inc. [kPa]
1	383	2.5	31
2	414	5	-60
3	354	5	60
4	414	5	-60
5	354	5	60
6	414	5	-60
7	354	5	60
8	414	5	-59
9	355	5	59
10	414	5	-55
11	359	5	54
12	413	5	-53
13	360	5	52
14	412	5	-49
15	363	5	46
16	409	5	-38
17	371	5	32
18	403	5	-26
19	377	5	20
20	397	5	-17
21	380	5	15
22	395	5	-15
23	380	5	14
24	394	5	-13
25	381	5	13
26	394	5	-13
27	381	5	12
28	393	5	-12
29	381	5	12
30	393	5	-12
31	381	5	12
32	393	5	-11
33	382	5	10
34	392	5	-11
35	381	5	11
36	392	5	-10
37	382	5	56.5333

The comparisons of the laboratory test and the PLAXIS SoilTest are illustrated in Figure 4.9 . As it can be seen the excess pore pressure follows each other nicely in the first 50 s, where the

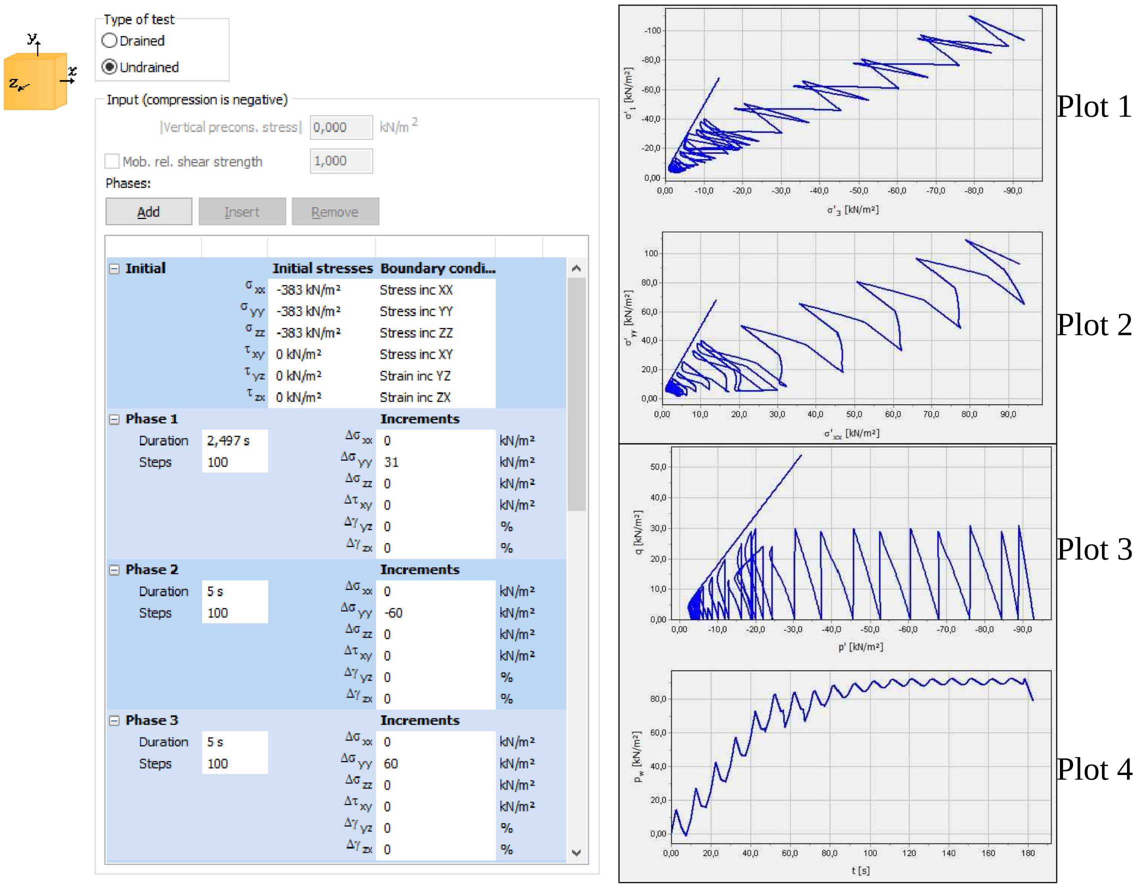

Type of test

○ Drained

● Undrained

Input (compression is negative)

|Vertical precons. stress| 0,000 kN/m²

☐ Mob. rel. shear strength 1,000

Phases:

Add Insert Remove

Initial	Initial stresses	Boundary condi...
σ_{xx}	-383 kN/m²	Stress inc XX
σ_{yy}	-383 kN/m²	Stress inc YY
σ_{zz}	-383 kN/m²	Stress inc ZZ
τ_{xy}	0 kN/m²	Stress inc XY
τ_{yz}	0 kN/m²	Strain inc YZ
τ_{zx}	0 kN/m²	Strain inc ZX

Phase 1		Increments		
Duration	2,497 s	$\Delta\sigma_{xx}$	0	kN/m²
Steps	100	$\Delta\sigma_{yy}$	31	kN/m²
		$\Delta\sigma_{zz}$	0	kN/m²
		$\Delta\tau_{xy}$	0	kN/m²
		$\Delta\gamma_{yz}$	0	%
		$\Delta\gamma_{zx}$	0	%

Phase 2		Increments		
Duration	5 s	$\Delta\sigma_{xx}$	0	kN/m²
Steps	100	$\Delta\sigma_{yy}$	-60	kN/m²
		$\Delta\sigma_{zz}$	0	kN/m²
		$\Delta\tau_{xy}$	0	kN/m²
		$\Delta\gamma_{yz}$	0	%
		$\Delta\gamma_{zx}$	0	%

Phase 3		Increments		
Duration	5 s	$\Delta\sigma_{xx}$	0	kN/m²
Steps	100	$\Delta\sigma_{yy}$	60	kN/m²
		$\Delta\sigma_{zz}$	0	kN/m²
		$\Delta\tau_{xy}$	0	kN/m²
		$\Delta\gamma_{yz}$	0	%
		$\Delta\gamma_{zx}$	0	%

y
x
z
Plot 1
σ'1 [kN/m²]
-100
-80,0
-60,0
-40,0
-20,0
0,00
0,00 -10,0 -20,0 -30,0 -40,0 -50,0 -60,0 -70,0 -80,0 -90,0
σ'3 [kN/m²]
Plot 2
σ'yy [kN/m²]
100
80,0
60,0
40,0
20,0
0,00
0,00 10,0 20,0 30,0 40,0 50,0 60,0 70,0 80,0 90,0
σ'xx [kN/m²]
Plot 3
q [kN/m²]
50,0
40,0
30,0
20,0
10,0
0,00
0,00 -10,0 -20,0 -30,0 -40,0 -50,0 -60,0 -70,0 -80,0 -90,0
p' [kN/m²]
Plot 4
pw [kN/m²]
80,0
60,0
40,0
20,0
0,00
0,00 20,0 40,0 60,0 80,0 100 120 140 160 180
t [s]

Figure 4.7: *Screen shot from PLAXIS SoilTest.*

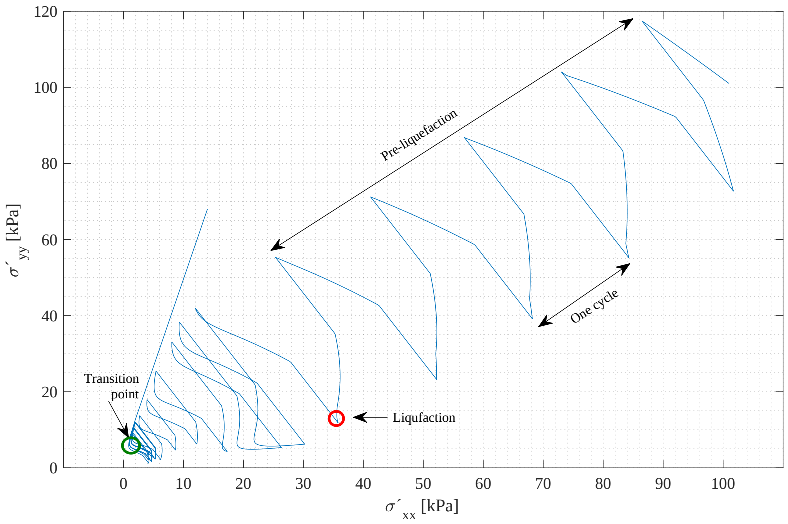

Figure 4.8: *Output plot of the effective stresses from PLAXIS SoilTest.*

SoilTest shows a slightly smaller convergence value of $\Delta p_w \approx 98\,\text{kPa}$ than the laboratory with a convergence valus of $\Delta p_w \approx 102\,\text{kPa}$. In the same way, the number of cycles needed in the elastic phase before initiation of liquefaction is the same for both the SoilTest and the laboratory test, although there is a slight offset between the peaks. The effective stresses almost reach a value

Table 4.2: *Effects of increasing the stiffness parameters in the soil model UBC3D-PLM.*

Parameter	Description of effect	Best fit
K_B^e	The pre-liquefaction phase becomes shorter with a few cycles before liquefaction occurs. The soil becomes softer faster and cycles increase in fluctuations. The excess pore pressure increase rapidly to a stady value of $\approx \sigma'_{v0}$.	150
K_G^e	Similar effect as K_B^e with a decrease of number of cycles in the pre-liquefaction. An increase in value has little effect on the excess pore pressure development (plot 3)	180
K_G^p	The numbers of cycles increase in the pre-liquefaction. The excess pore pressure develops slowly and does not reach in proximity $\sigma_{v'0}$. This indicate that for consolidated soil the parameter needs to relatively high.	350
me, ne	Similar effect as K_G^p with an increase in the number of cycles in the pre-liquefaction. More cycles are needed before liquefaction happens. The parameter has little effect on the development of the excess pore press. The parameter can be used to tweak the pre-liquefaction phase by adjusting the frequency of the cycles (the "space" between cycles).	0.7, 0.5
np	The transition from the cyclic phase to the monotonic post-liquefaction phase becomes more sharp and turns to give an increase in both the mean effective stress and the deviatoric stress, where the mean effective stress will continue to decrease for a smaller value of np.	1
f_{dens}	The inclination on the reloading branch for the cycles increase. The maximum excess pore pressure decreases and the minimum mean effective stress and deviatoric stress increases and does not reach zero.	0.2
f_{Epost}	No detectable effects in either plots.	0.6

of 0 kPa at the transition point, whereas for the laboratory test the effective stresses go beyond zero. The post-liquefaction stage (monotonic stage) have though the same inclination for both curves meaning that the increment of effective stress regeneration is the same. The calibration is achieved rather manually by changing one parameter at a time according to Table 4.2 . Thus, a better calibration could be achieved by continue tweaking the parameters, but for the scope of the project the attained values are deemed close enough, since the main focus is the build up of the excess pore pressure.

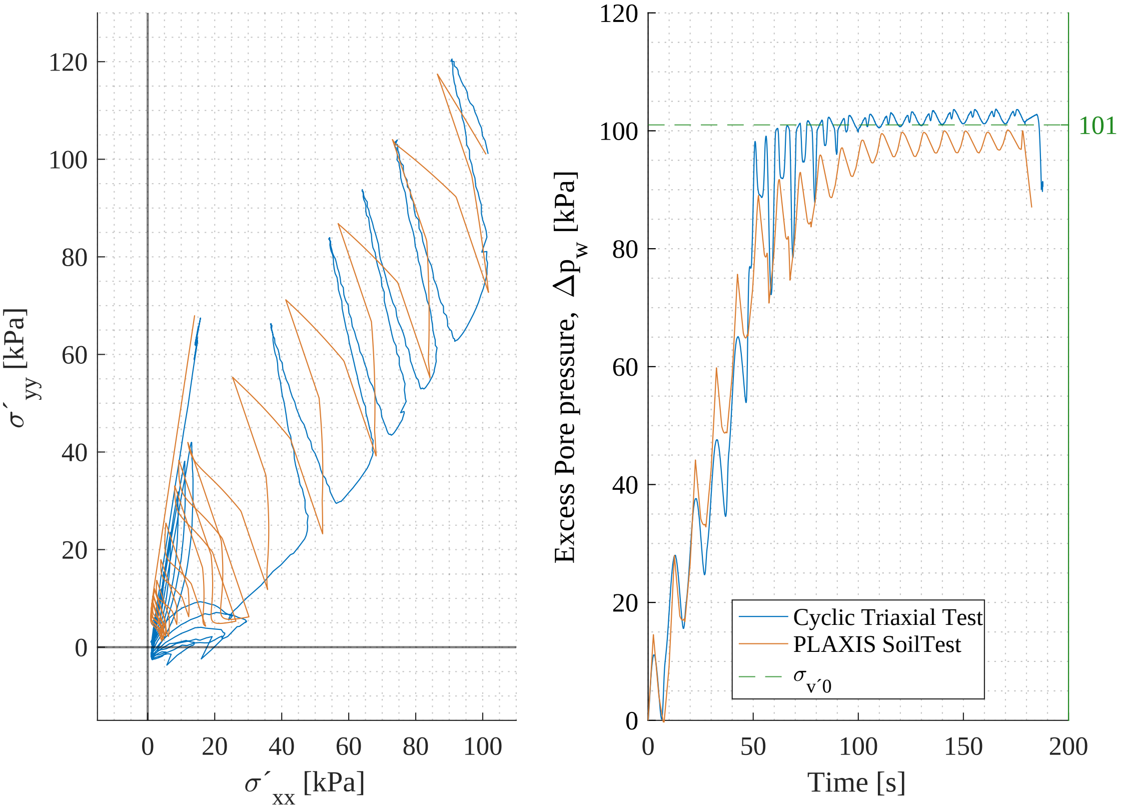

Figure 4.9: *Comparison between the laboratory test and the SoilTest in PLAXIS with stiffness parameters set as in Table 4.2*

Chapter 5

Numerical setup

The simulation of a monopile situated in liquefiable soil is carried out in the program PLAXIS 3D, which is a finite element program capable of representing a broad range of soil behaviours by utilizing different constitutive relations for different soil deposits. As with any other finite element program the user takes control of almost all input parameters and settings and thus the outcome is highly sensitive to how geometric dimensions, boundaries, mesh refinement etc. are defined.

5.1 From reality to conceptual model

The complexity of the reality in a geotechnical problem is often far too great to be modelled in details, so it is necessary to abstract the reality into a conceptual model that can be transformed into a computer model (Brinkgreve, 2013). The small series of figures in Figure 5.1 is to illustrate this process of going from a real physical setup to a simplified conceptual model and then to a computer simulated model. In figure A) an example of the in situ conditions are roughly illustrated with irregular strata of soft sand layer, stiff sand layer and a bottom rock layer. At great depth a hypocenter is illustrated with a red star and through the soil layers the resulting stress waves propagation are symbolized by half-circles. In figure B) the reality is crudely cropped down and simplified into a conceptual model of the most interesting part of the soil domain. The strata is depicted with linear transition at the seabed and between the soil deposits contrary to the real strata composition shown in figure A). The reflection of the stress waves when hitting the monopile are schematic shown with smaller half-circles. In figure C) the boundaries of the conceptual model are altered in order to take into account the cropped out soil, so the computer model simulates the reality in an optimal way. As the stress waves continue in infinity the boundaries need to absorb the stress waves rather than reflecting them back into the soil domain. This is mechanically overcome by attaching dashpots to the vertical and bottom edge. The dynamic impulse from the hypocenter is replaced by a dynamic horizontal displacement indicated with double arrows. The origin of stress wave propagation is therefore no longer focused at one point in space, but spread out of the whole bottom boundary. The propagation of stress waves in the soil domain are now represented by curly lines.

The restrictions on the cropped reality and the different boundary conditions available in PLAXIS are further discussed in the following sections.

5.2 Geometric dimensions

The overall geometric dimensions of the model need to be of such a magnitude that the full mesh deformation is captured in all directions, but no more than that in order to limit extensive calculation time. For a static 2D case there exist some guidelines for the model size based on structure

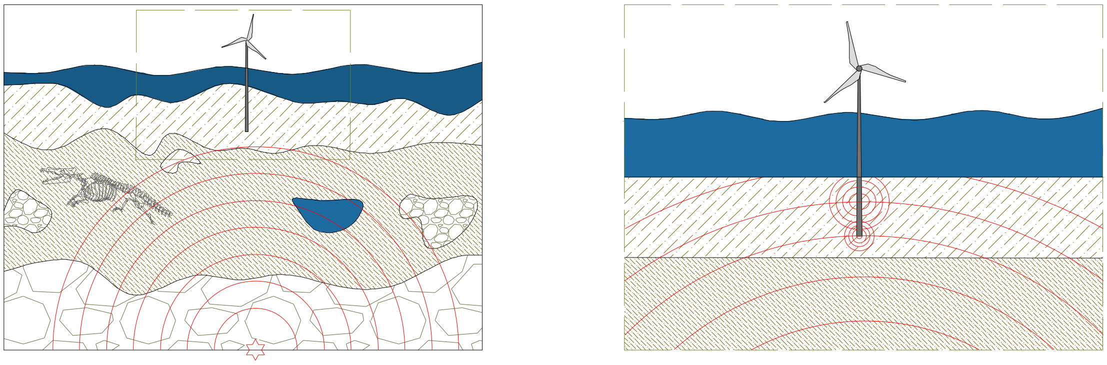

A) Sketch of how in situ conditions could look like. The red half-circles symbolizes stress waves propagation from the hypocenter marked with a red star.

B) Idealized representation of in situ condition used for further modelling. The smaller stress waves are reflections when the primary stress wave impact the structure.

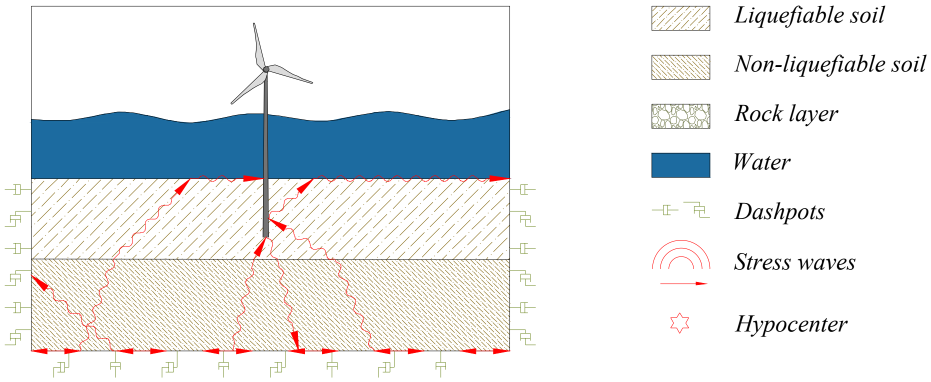

C) Simplification of the idealized model as it is modelled in PLAXIS 3D. On the edge of the rectangle are small dashpots representing the free-field boundary condition and the complian base. Each dashpot is attached to a node in the model. At the base the primary stress waves are replace by a horizontal movement, here represented with double arrows. The curly lines are the propagation of the stress wave through out the main soil domain.

Figure 5.1: *Schematic drawing of the process going from reality to a computer model in PLAXIS3D.*

dimensions (Brinkgreve, 2013). However, since this is a dynamic 3D analysis, the boundaries should be further away than for a static analysis, because otherwise there is a risk of distortion in the results from reflected stress waves at the boundaries. To overcome this, special boundary conditions can be applied to reduce the model size, so the controlling parameter is not the necessarily the dynamic load, but more a static load. Unfortunately, it is still not possible to calculate the exact dimensions of the model, so an iterative process is required. This process is illustrated in the flowchart in Figure 5.2 , where the first step is to guess on initial dimensions. After the initial guess the actual iteration starts indicated with the red and blue loops. At the end of the calculation the results are assessed and if the relative mesh deformation interacts with the boundaries the model needs to be extended (red loop). Contrary, if mesh deformation ceases not too close to boundaries it could be advantaged to abridge the model (blue loop). Ideally, the model should be of such a size that the boundaries just precisely does not influence the deformation of the monopile (R.B.J Brinkgreve, 2017).

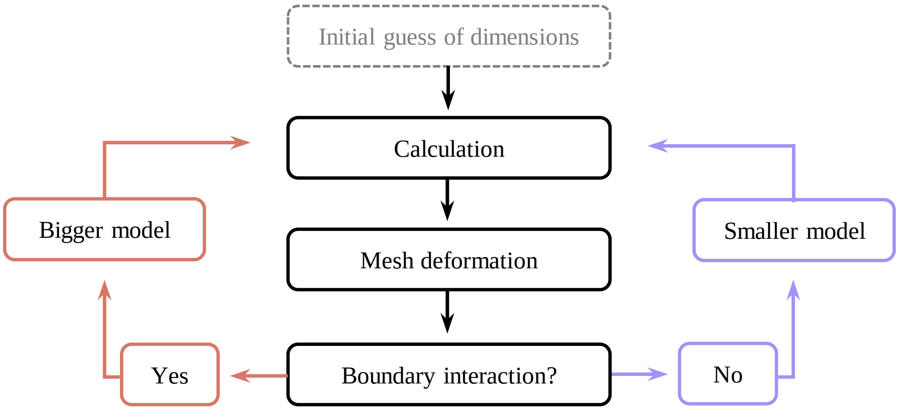
Initial guess of dimensions
Calculation
Mesh deformation
Boundary interaction?
Yes
No
Bigger model
Smaller model

Figure 5.2: *Iterative process to determine the overall geometric dimensions.*

In the case investigated the monopile is only situated in the top liquefiable layer. The case is illustrated in Figure 5.3 with the overall model dimensions. The part of the pile above seabed is set to 15 m. The object is to investigate the pile displacement and the soil resistance in an effort to establish a p-y curve for post-liquefaction.

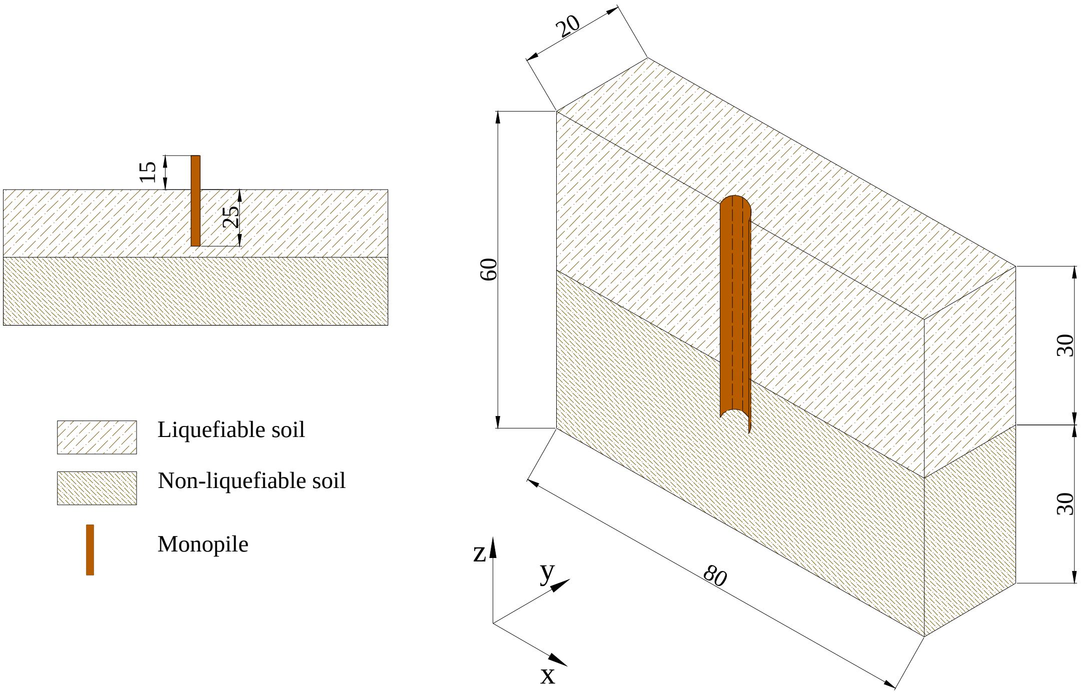
15
25
Liquefiable soil
Non-liquefiable soil
Monopile
20
60
30
30
80
z
y
x

Figure 5.3: *Illustration of the case investigated. All dimensions are in meter.*

5.3 Boundary conditions

As described in the previous section, when dealing with a dynamic analysis there is a risk of reflecting the stress waves back into the model domain at the boundaries and thereby distort the computed results. Therefore, the boundaries need to be manipulated in such a way that the behaviour of the model reflect the reality in the best way.

PLAXIS3D offers three different boundary conditions for a dynamic analysis, each designed to simulate a certain reality and behaviour:

1. *Viscous boundaries* utilizes viscous dampers instead of fixities in a particular direction. The dampers work by absorbing the stresses on the boundary without rebounding the stress waves back into the main domain. The dampers can absorb stresses from both P- and S-waves as illustrated in Figure 5.4 . In the figure both the vertical and horizontal damper are attached to the same node, but only the green damper is active for the respective stress wave. This type of boundary setting is suitable when the dynamic source is inside the soil domain.

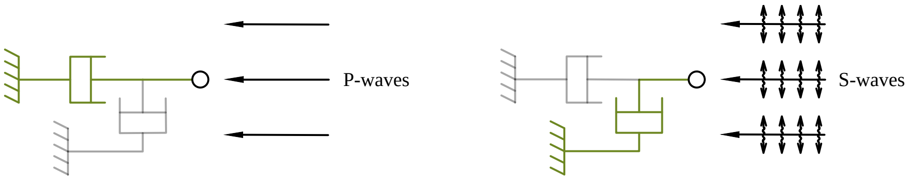

Figure 5.4: *Viscous boundaries. Normal and shear dashpot, respectively.*

2. *Free-field boundaries* are suitable when the dynamic source is applied as a boundary condition (such as a prescribed displacement). The motion of the free field is applied to the boundaries by free field elements that are connected to the main domain by viscous dashpots. The wave propagation through the free field element behaves in the same way as the surrounding soil element in the main domain. The equation for the stresses in the free-field elements include effects of viscous boundaries to absorb waves reflected from internal structures.
3. In the case the boundary needs to both absorb and apply the dynamic input *Compliant base boundaries* can be used.

With these three types of boundary settings PLAXIS suggests to apply the free-field boundaries at x_{min} and x_{max} and the compliant base at the bottom boundary at z_{min} when the dynamic load stems from an earthquake impulse. At y_{min}, y_{max} and z_{max} the boundary condition is set to *Free*.

5.4 Structure creation

Creation of monopile

To limit the amount of elements in the whole model the symmetri of the pile around its longitudinal axis is utilized and thus only half the pile is modelled. The pile is then modelled in the following way:

1. Extrude a polycurve with a radius of $r_{monopile} = 4\,\text{m}$ from $z = 0\,\text{m}$ downward to the desired depth thus making a surface resembling half the monopile.
2. Make the surface into a plate and give the plate the steel properties shown in Table 5.1 .

Table 5.1: *Parameters for the steel pile modelled in PLAXIS.*

Diameter	Thickness	E-modulus	Poisson's ratio	Density
8 m	0.1 m	205 GPa	0.3	7859 $\text{kg}\,\text{m}^{-3}$

3. Apply interfaces on both sides of the plate structure for better calculate soil-structure interactions. In the post process the data are extracted from nodes on the interfaces rather in the plate or soil elements themselves.

4. A helper object is defined around the monopile to refine the mesh in this region, since stress concentrations are expected to be in the vicinity of the plate structure and interfaces. This is merely a numerical trick to focus the density of the mesh, and thereby the precision of the calculations, on the most critical part of the model. The helper object is made with a polycurve of $r = 3 \times r_{monopile}$.

Application of loads

The earthquake load is applied as a prescribed displacement at the bottom edge, cf. Figure 5.1 . The input is a time series of ground acceleration of the 1990 Upland Earthquake with a magnitude of $M_L = 5.5$ (on the Richter scale) provided by USGS and is suggested by PLAXIS. A time series of the ground acceleration is seen in Figure 5.5 .

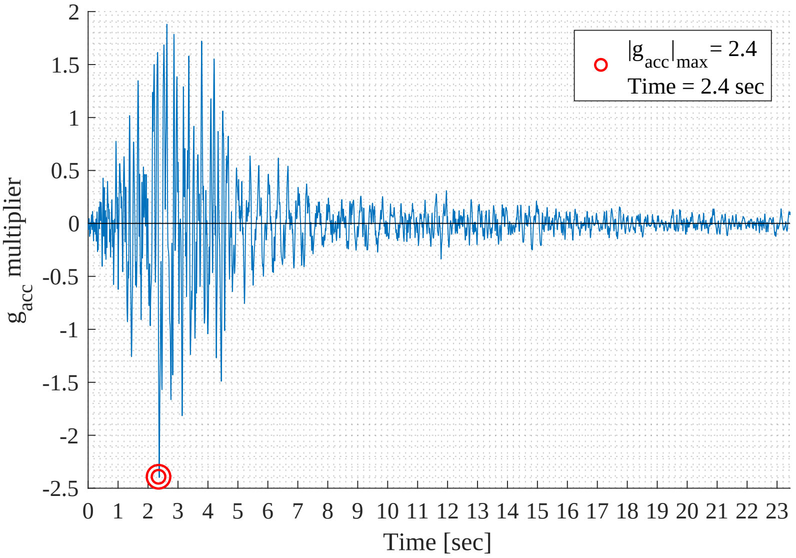

Figure 5.5: *Time series of ground acceleration.*

The time step of the signal is $\delta t = 0.005\,\mathrm{s}$ and the whole signal consists of 4688 steps, which equate to a total time of $t = 23.44\,\mathrm{s}$. The peak ground acceleration (PGA) happens after 2.4 s and with an ground acceleration multiplier of $g_{acc} = 2.4$. After $\approx 8\,\mathrm{s}$ the ground acceleration subside in intensity

As an addition to the dynamic prescribed displacement a static prescribed displacement is added to the monopile. This static displacement is activated after the earthquake have happened. The magnitude of the static prescribed displacement is set to $u_{stat} \geq 1.5\,\mathrm{m}$.

5.5 Soil parameters

For the liquefiable soil layer the soil parameters are determined in Chapter 4 by a calibration from the cyclic triaxial test. The complete set of soil parameters for both layers are listed in Table 5.2

5.6 Mesh generation

To further limit excess computation time the amount of nodes needs to be kept at such a level that further refinement of the mesh only produces slight changes in the result. Since the number of nodes directly controls the number of equations to be solved it is imperative to carefully chose a minimum refinement degree, so the overall computation time is reduced as much as possible, but still produce acceptable results. This threshold is determined by a convergence analysis by slightly

Table 5.2: *Material parameters for both the two layers used in the case.*

	Liquefiable layer	**Non-liquefiable layer**	
Material model	UBC3D-PLM	Hardenin Soil	
Drainage type	Undrained A	Drained	
γ_{unsat}	18	20	
γ_{sat}	20	20	
k_B^e	150	E_{50}^{ref}	30.000
k_G^e	180	E_{oed}^{ref}	36.010
k_G^p	350	E_{ur}^{ref}	110.800
me	0,7	power	0,5
ne	0,5		
np	0,5		
ϕ_{cv}	30	ϕ'	28
ϕ_p	40	ψ'	0
c	0	c_{ref}	5
σ_t	0		
$N_{1,60}$	5		
f_{dens}	0,2		
f_{Epost}	0,6		
R_f	0,9		

increasing the fineness of the soil cluster encapsulated by the helper object around the monopile. In Figure 5.6 is shown the final mesh refinement for the case, where the colors indicate the relative coarseness. On the right side of the figure is a colorbar with indication of coarseness. The top soil layer is split into two clusters, where cluster 1.2 is the soil cluster encapsulated by the helper object and consist of both the soil inside and outside the monopile. The bright purple dot at the corner of the monopile represent the node at which mesh convergence is investigated for. For a proper convergence to be done it is beneficial to chose a node that will always be placed at the exact same place in space and is highly imporant for the results, and since the structure of the mesh is forced to have nodes at the boundaries of entities there will always be a node where the monopile intersects the soil.

5.6.1 Convergence analysis

In Table 5.3 the systematic refinement of soil cluster 1.2 for the case is listed.

Table 5.3: *Coarseness factor. Cf. Figure 5.6 for soil clusters.*

Iteration	Soil cluster 2	Soil cluster 1.1	Soil cluster 1.2	Boundaries	Pile	Number of nodes	$\lvert u\rvert_{soil} [m]$
1	1,0	1,0	1,5	0,5	0,5	25.108	0,0230
2	-	-	1	-	-	26.662	0,0220
3	-	-	0,7	-	-	31.073	0,0207
4	2,0	2,0	0,5	0,5	0,5	39.130	0,0202
5	-	-	0,3	-	-	62.397	0,0205

In Figure 5.7 the displacement for each iteration for the case is plotted to give a better overview. The first plot shows the displacement for each iteration, and while the slope clearly decreases towards the fifth iteration, it is the relative difference between two successive iteration that determines when a convergence is acceptable. This is shown in the second plot, where the difference between

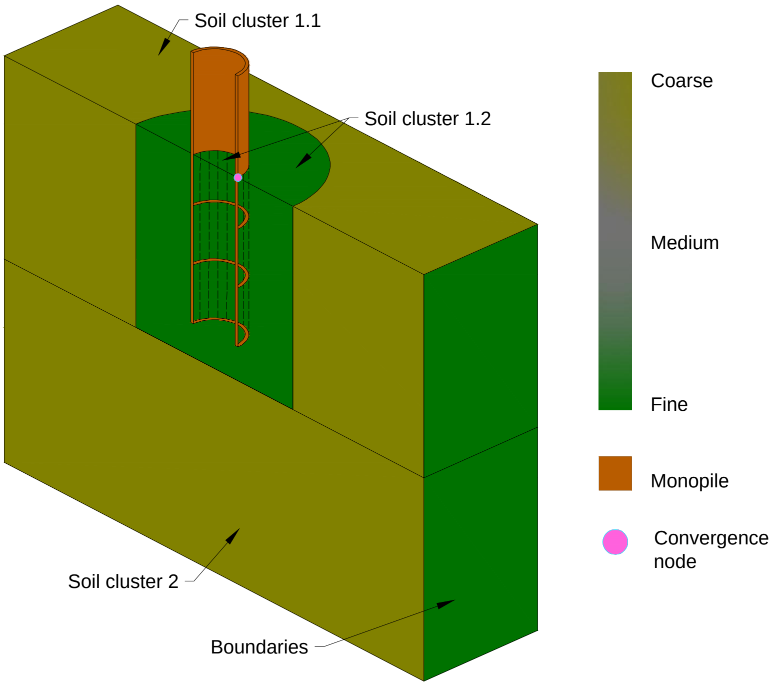

Figure 5.6: *Relative refinement for the final iteration.*

the preceding and the current note is plotted. The difference between the second and first iteration is 4.55 %, while the difference between the third and second is 6.28 %. From the fourth to the fifth iteration the difference between the displacement $|u|$ is only 0.98 %. Any more refinement of the mesh will only produce a slight difference in displacement, and so the forth iteration is chosen as the convergence iteration. The final coarseness used in the further analysis is highlighted in Table 5.3 .

5.7 Calculation

The calculation is set up in three distinct phases in the following order:

1. **Initial phase**. A default phase in PLAXIS3D to set initial stresses in the soil.
2. **Pile installation**.
3. **Phase 1 (earthquake)**. After the initial phase the earthquake excitation is simulated by a dynamic analysis. Since the free field elements and the compliant base is used at the boundaries it is crucial that an interface is applied at boundaries to activate the boundary conditions.
4. **Phase 2 (static displacement)**. After the simulated earthquake load the static prescribed displacement is activated while the dynamic prescribed displacement is deactivated. The phase is calculated as a *plastic* calculation.

In all the phases the default calculation settings are valid except in the dynamic calculation, where the number of max steps and sub steps need to fulfill the following equality:

$$\Delta t = \delta t(m \cdot n)$$

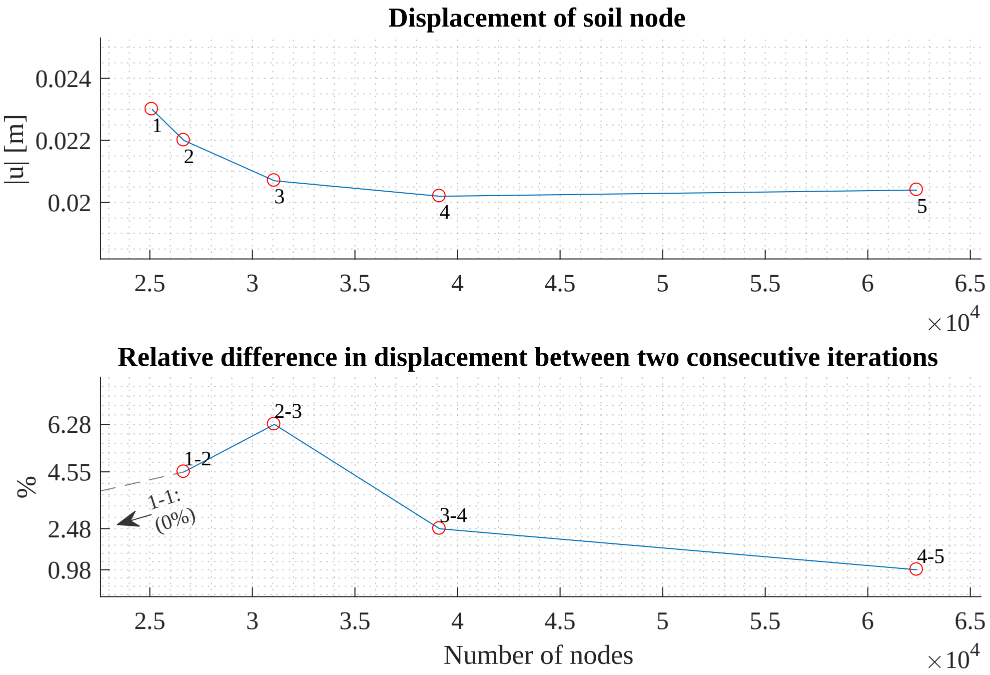

Figure 5.7: *Convergence plot for the case.*

Δt	Duration of dynamic loading (Dynamic time interval).
δt	Time step. This is equal to the time step of the signal used as input load.
m	Number of steps.
n	Number of sub steps.

Chapter 6

Results

In the following chapter the results from the case discussed in Section 5.2 is presented. As the main purpose of the soil model is to determine the build up of excess pore pressure and the initiation of liquefaction the development of the excess pore pressure ratio r_u through the earthquake will be shown. Furthermore, the movement of the monopile for different time steps will be shown to ease the understanding of the impact from the earthquake. At the end of the dynamic phase a static analysis is conducted with a predescribed lateral displacement on the whole pile of 1.5 m. This analysis is done to establish a relation between the post-liquefied shear strength at different depth and eventually a p-y relation.

Description of the excess pore pressure ratio

The excess pore pressure ratio r_u is a factor that is used to determine the onset of liquefaction. As described in Chapter 3 when the excess pore pressure equalizes the effective stresses liquefaction occurs.

In Kramer (1996) and Lombardi et al. (2014) the excess pore pressure ratio is defined as

$$r_u = \frac{\Delta p_w}{\sigma'_{3,c}} \tag{6.1}$$

Here the effective stress in the denominator is taken as the initial effective confining pressure from a triaxial compression test, $\sigma'_{3,c}$.

In PLAXIS the excess pore pressure ratio can be defined in two ways

$$r_{u,\sigma' v} = 1 - \frac{\sigma'_v}{\sigma'_{v0}} \tag{6.2}$$

$$r_{u,p'} = 1 - \frac{p'}{p'_{v0}} \tag{6.3}$$

σ'_v	Vertical effective stress at the end of the dynamic calculation
σ'_{v0}	Initial effective stress prior to the seismic motion
p'	Effective mean stress at the end of the dynamic calculation
p'_0	Initial effective mean stress prior to the seismic input

Both Eq. (6.2) and Eq. (6.3) give similar information about the onset of liquefaction, but is clearly different in the reference effective stress. With reference to Eq. (3.2) the former of the two definitions are used.

Furthermore, Beaty and Byrne (2001) emphasizes that momentary fluctuations of stress redistribution can lead to misinterpreted liquefaction. It is therefore suggested in Beaty and Byrne (2001) not to use the definition presented by Kramer (1996) and Lombardi et al. (2014), when r_u is used to distinguish between liquefied and non-liquefied zones. Additionally, Beaty and Byrne (2001) suggests to set a range for r_u as

$$\begin{array}{lcl} r_u = 0 & : & \text{No liquefaction} \\ r_u \geq 0.7 & : & \text{Onset of liquefaction} \end{array}$$

6.1 Results for the excess pore pressure ratio

The excess pore pressure ratio is extracted along five different "strings" located around the pile, see Figure 6.1 . The blue dots are nodes along a target soil coloumn that form these "strings". The identification for each string is located at the top of the string. In Table 6.1 the target coordinates for each string is listed.

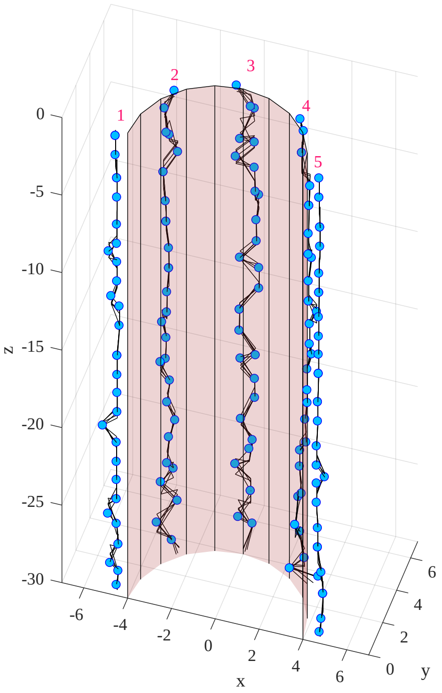

Figure 6.1: *Extraction "strings" from the PLAXIS model.*

In Figure 6.2 the increase in $r_{u,\sigma'v0}$ at different time steps is seen for string number 5. For the first 8 s r_u is plotted for every 0.5 s, and hereafter for every 1 s until the end of the dynamic calculation of 15 s. The red dotted line indicate the threshold to which liquefaction is at full. As it can be seen r_u increases rapidly in the first 3 s, where after only 2 s the first 1 m has surpassed the threshold. Identical trends can be seen for the other strings in appendix A. In appendix A is also shown screen shots at different time step of the dynamic calculation for $r_{u,\sigma'v0}$.

The average pore pressure ratio between the strings is shown in Figure 6.3. The liquefied zone extends down as the dynamic load proceeds and stagnates around a depth of $\approx 2\,\text{m}$ at the end of the dynamic calculation. Liquefaction has not developed at greater depth, but σ'_{v0} has decreased as $r_u > 0$ all the way to the bottom of the soil layer. In general, throughout the whole dynamic calculation the development of r_u follows the preceding ratio in a parallel manner. In the middle of

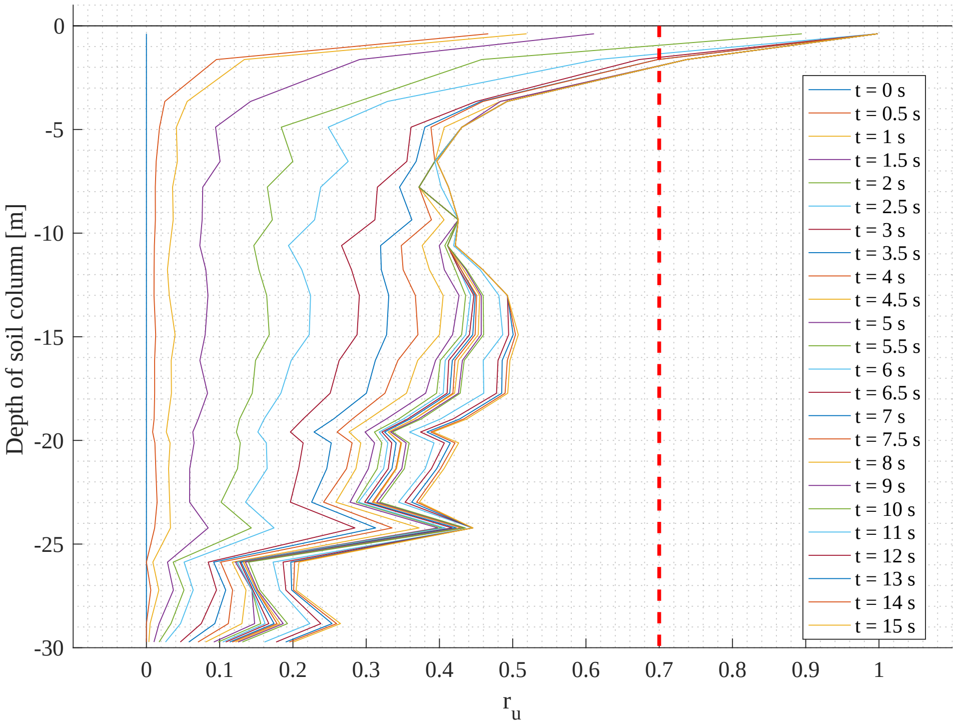

Figure 6.2: *r_u from $t = 0\,\mathrm{s}$ to $t = 15\,\mathrm{s}$ for string number 5.*

the soil column the excess pore pressure ratio increases a bit before is drops again in the last $\frac{1}{4}$ of the soil column (around $z = -20\,\mathrm{m}$).

Table 6.1: *Coordinates for each string in Figure 6.1*

String	X_{target}	Y_{target}
1	-4.5	0
2	-3	3
3	0	4.5
4	3	3
5	4.5	0

6.2 Pile displacement during earthquake load

In Figure 6.4 is shown the pile displacement at different time steps. The first subplot is after the pile has been installed, and in the succeeding subplots the shaded grey monopile is at the time of pile installation. For every time step the red displaced monopile can therefor be seen in reference to the initial pile installation. The general trend of the displacement is a downward movement and a tilting to the left in the first few seconds. At the end, after 14 s, the tilting has reduced and the monopile has a more upright position.

In Figure 6.5 is shown the same pile displacement, although the shaded grey monopile is now in reference to the previous time step. The relative displacement is significantly greater in the first 4 s, where it decreases further along the dynamic motion. The correlation between the build up of excess pore pressure, and thus the decrease in effective stresses, and the movement of the monopile is therefor in good agreement, as both the displacement of the monopile and the build of excess

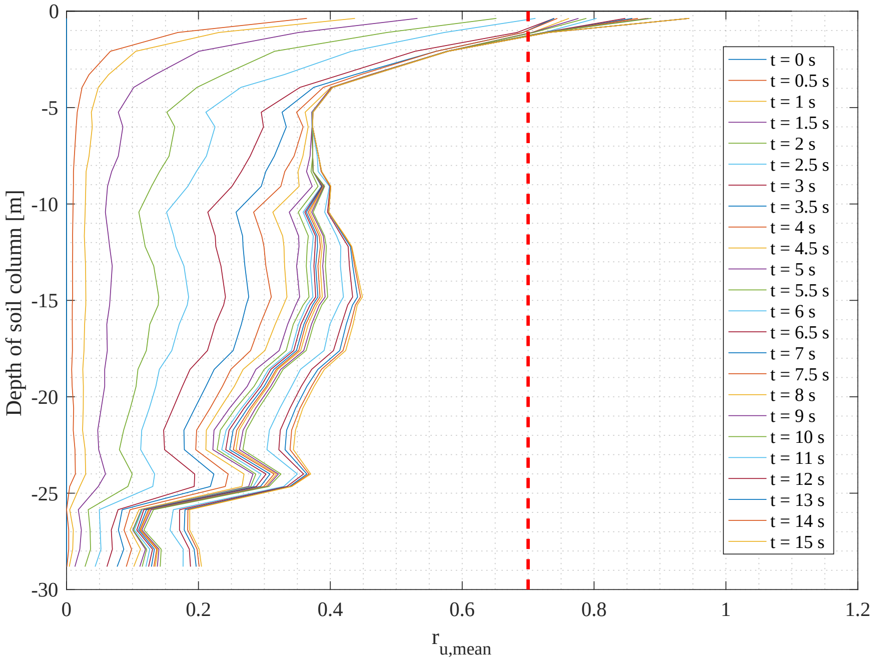

Figure 6.3: *Average value of r_u around the monopile for different time steps.*

pore pressure accelerates in the first few seconds and decelerates in the last few seconds of the dynamic calculation.

6.3 Post-liquefaction soil strength and stiffness

After the dynamic calculation has ended a static analysis is undertaken to investigate the residual shear strength and the relation between pile displacement and soil resistance - so called p-y relation. The calculation is carried out with the UBC3D-PLM soil model and the same input parameters as used in the dynamic calculation. The monopile is displaced 1 m laterally, and so no rotation occurs. The lateral displacement permit a better visualization of the residual soil strength all the way down the soil layer. Normal stresses, shear stresses and nodal displacement are extracted from the interface between the soil and the pile. A small script is made to convert the stresses in the stress points to equivalent soil resistances. The main idea behind the script is to divide the pile into sections and find the average normla- and shear stress for each section. This method is described in Wolf et al. (2013); Knudsen et al. (2013). The principal steps in the script is ;

1. Divide the pile into sections from predetermined number of rows and columns, so that $n_{sections} = rows \times coloumns$.
2. Find the average normal- and shear stress for each section between the stress nodes that are in the section.
3. Calculate forces in each section from the average stress and determine the force component along the displacement of the pile. Divide the force by the section height.
4. Calculate the resultant pressure between the passive and active pressure (active pressure pushes on the pile in the direction of movement).

The code has been verified by a simple lateral displacement of drained Mohr-Coloumb soil. The generated p-y relation for the verification analysis can be seen in appendix B.

The normal- and shear stresses at the end of the static analysis, when the pile has displace 1 m,

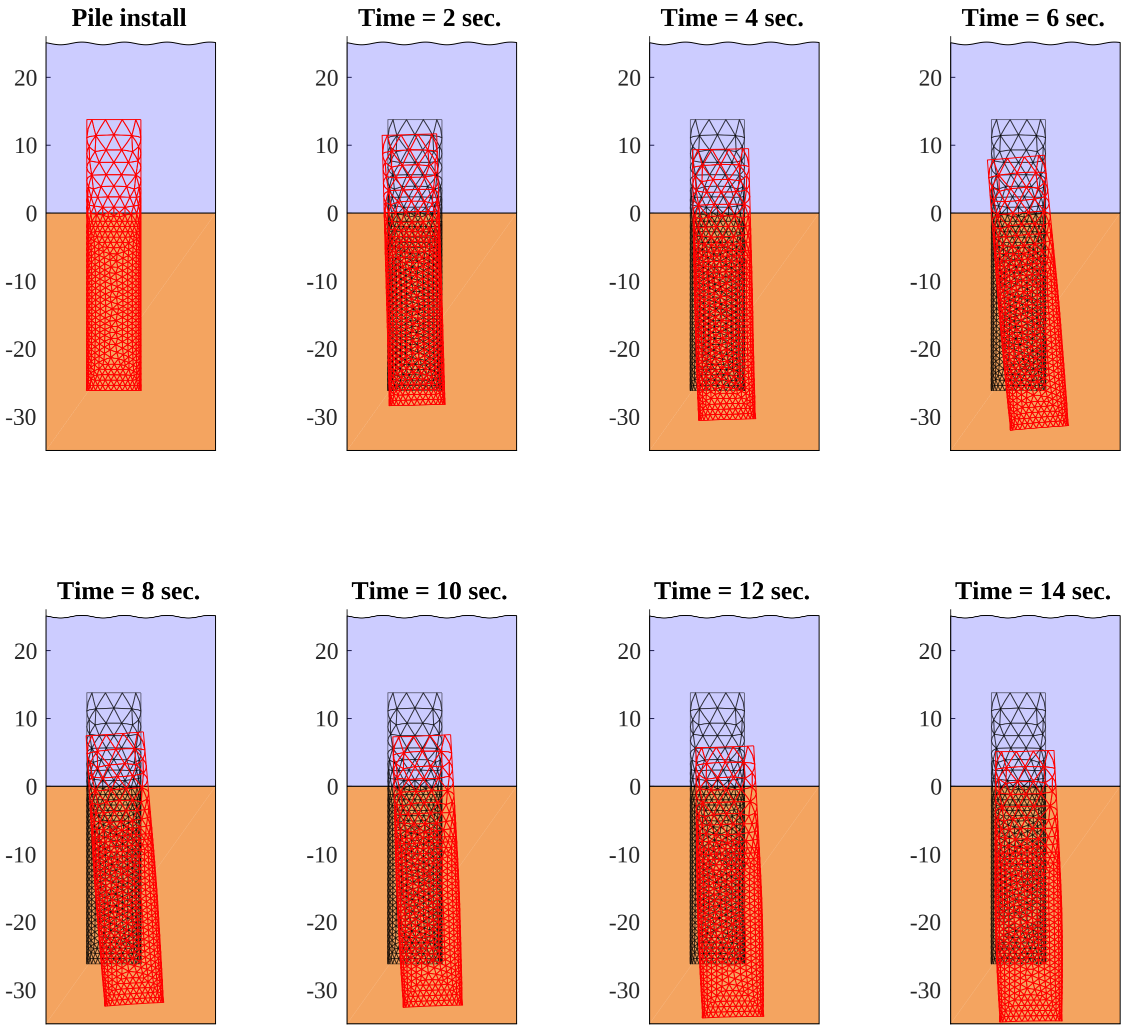

Figure 6.4: *Displacement of monopile with reference to the start of the dynamic calculation. The displacement is scaled by a factor of 300.*

is shown in Figure 6.6. The stresses are calculated in Gauss points, but are extrapolated out to the nodes, and in the figure the color indicate the magnitude of the stress according to the colorbar.

In Figure 6.7 the section division for case is shown. There is six rows and seven columns which gives a total of 45 sections. Each section is 4.6 m high.

The resulting p-y curves is shown in Figure 6.8 for the first five curves. As there is a stress concentration at the bottom of the pile, c.f Figure 6.6, the p-y curve generated from these stresses are discarded as they do not show the true relation between the soil resistance and pile displacement.

From Lombardi et al. (2017); Sivathayalan and Yazdi (2004); Dash et al. (2017) the post-liquefaction strength and stiffness is of limited character. The post-liquefaction stage, from the triaxial test c.f chapter 4, the shear stress-shear strain relation is viewed as a upward concave curve with a low stiffness G_1 at small shear strains, see Figure 6.9. At some point, the soil body starts to dilate creating cavitation in the pores, thus reducing the pore pressure and increasing the effective stress. The shear stresses starts to increase leading to a stiffness G_2 that is much higher than the initial stiffness G_1. From the monotonic test the initial stiffness is $G_1 = 2\,\text{kPa}$ and $G_2 = 26\,\text{kPa}$

According to Figure 6.3 liquefaction occurred approximately in the top 2 m. The p-y curve at this depth has a slight upward concave curve illustrated by the black dotted line in Figure 6.8 that

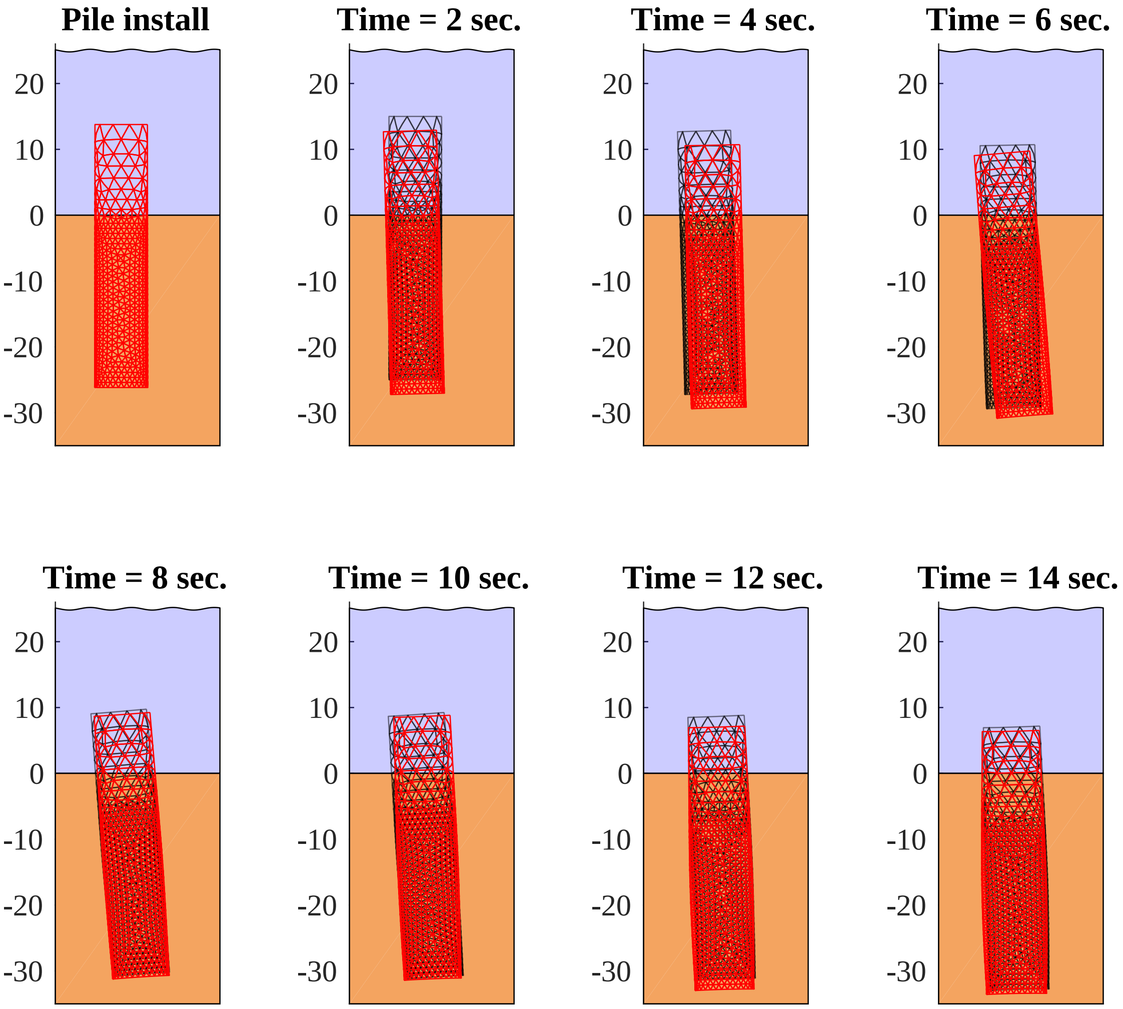
Pile install
Time = 2 sec.
Time = 4 sec.
Time = 6 sec.
Time = 8 sec.
Time = 10 sec.
Time = 12 sec.
Time = 14 sec.
20
10
0
-10
-20
-30

Figure 6.5: *Displacement of monopile with reference to the previous time step of the dynamic calculation. The displacement is scaled by a factor of 300.*

can resemble the initial part of the curve in Figure 6.9. However, there is no clear indication of increasing stiffness at the last displacement of 1 m. Further down in the soil where liquefaction has not developed the p-y curves resembles more those of the reference model, c.f Appendix B.

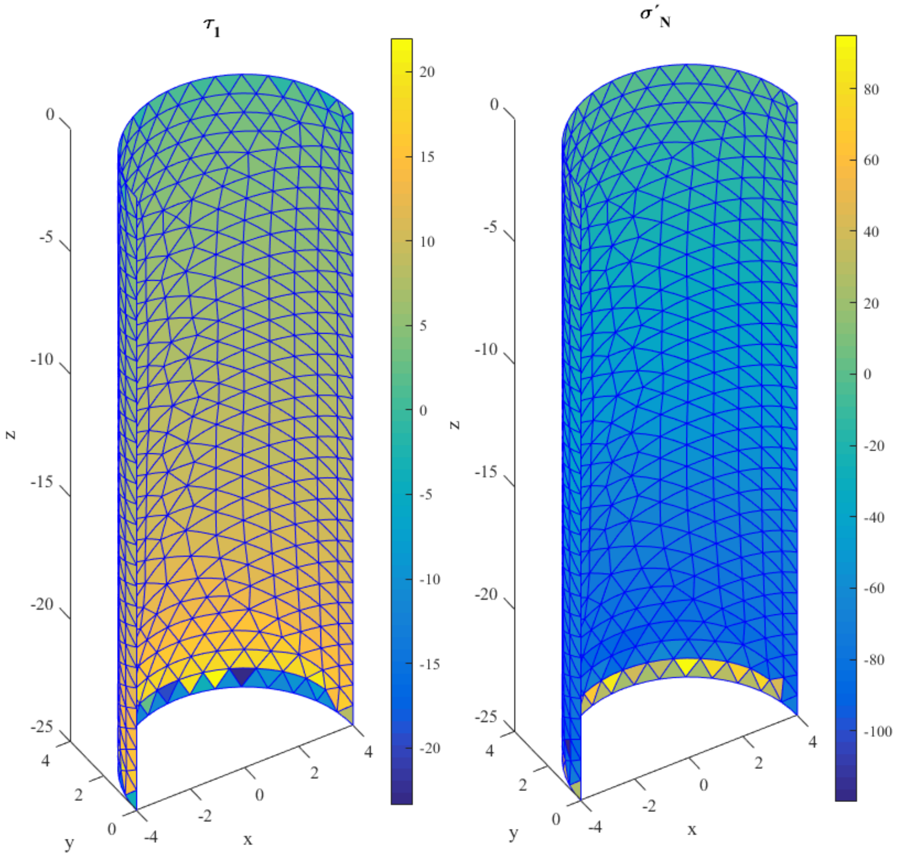

Figure 6.6: *Effective normal- and shear stresses on the pile at the end of the static analysis.*

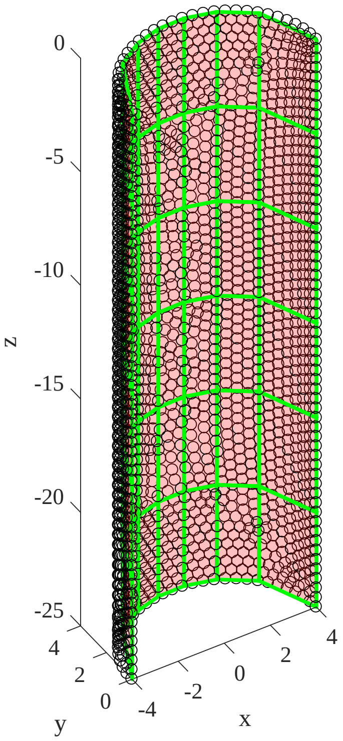
0
-5
-10
-15
-20
-25
z
4
2
0
y
-4
-2
0
2
4
x

Figure 6.7: *Division of monopile into sections for.*

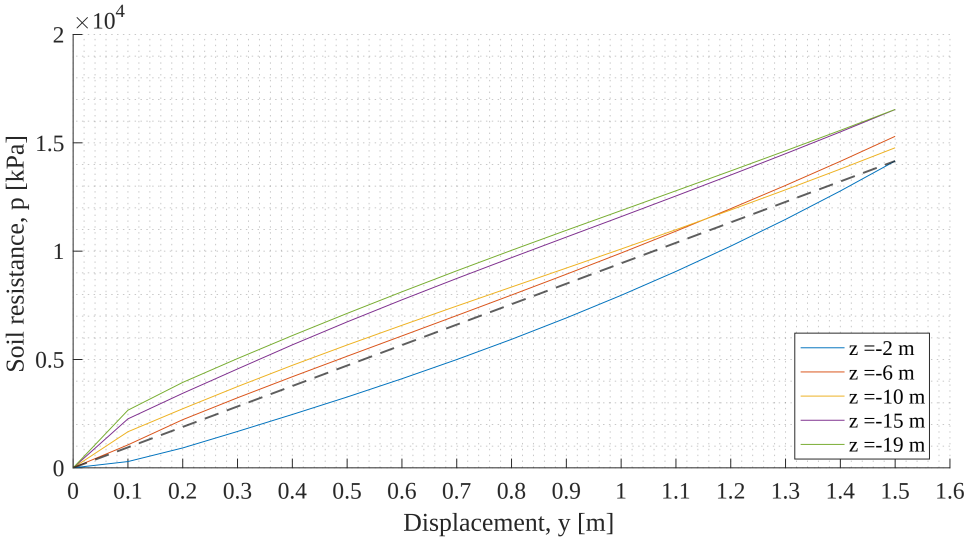

Figure 6.8: *P-y curves in the middle of the first five sections.*

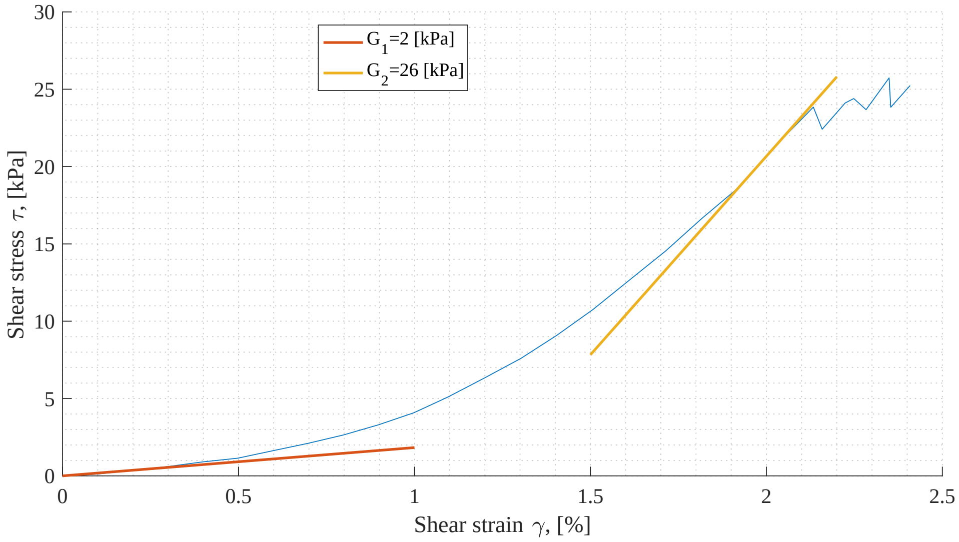

Figure 6.9: *Relation for post-liquefaction shear stress-shear strain. G_1 is the initial stiffness, while G_2 is the stiffness after the soil has gained effective strength. The curve is obtained from the multistage triaxial test.*

Chapter 7

Final Remarks

The results through out the report is firstly discussed with emphasis on limiting conditions and versatility of methods and models. The perspective of this discussion is from a practical point of view, where the applicability to real design cases and practical consequence on offshore foundation is the driving aspect. Following the discussion is a conclusion on the scope of the project and the main results.

7.1 Discussion of results

7.1.1 Calibration of the soil model

The calibration of the stiffness parameters and advanced parameters were done in the in-build feature of PLAXIS3D called SoilTest. The SoilTest facility enables the possibility to simulate conventional laboratory test (monotonic triaxial test, oedometer etc.) along with a *General* option to define arbitrary stress and strain conditions. As the laboratory test is a multistage cyclic triaxial test the *General* option is used.

The development of excess pore pressure (EPP) from the material model UBC3D-PLM showed very good agreement with the development of EPP in the laboratory test for the first 20 s, but showed a bit higher EPP after the first 20 s, c.f Figure 7.1. The stagnation EPP at the end of the test from the material model was a bit lower than that of the laboratory test by 4 kPa, but with a EPP ratio larger than 0.7 for both test liquefaction has occurred when EPP starts to stagnate. An even better calibration could have been reached by changing the soil parameters slightly, and with the big difference in the calibrated parameters from the ones in but the final calibrated parameters are evaluated as sufficient based on the comparison in Figure 7.1.

7.1.2 Case results

From the case investigated the excess pore pressure and the post-liquefaction shear strength will be discussed.

Excess pore pressure and excess pore pressure ratio

The increase of EPP, and thus the decrease of effective strength, is seen as a top-down trend by the EPP ratio, that happens in the first few seconds of the dynamic load. The average extent of the liquefied zone was limited to a depth of $\approx 2\,\mathrm{m}$ below seabed by the EPP ratio. After $\approx 4.5\,\mathrm{s}$ the intensity of ground acceleration strongly decreases and this can be seen in the rate by which r_u develops. In Figure 7.2 the maximum rate of $r_{u,\sigma'v0}$ occurs at 2.5 s which is the time the peak ground acceleration happens, c.f Figure 5.5. After 5 s there is practically no change in $r_{u,\sigma'v0}$.

From a practical perspective the consequence of low effective stresses is a reduced shearing strength and stiffness of the soil in the top layer. The lateral support for a pile foundation is thus highly affected by the low residual effective stresses and stiffness. Great deflection must be expected to occur in the time after the earthquake if the wind turbine is affected by a significant vertical load e.g from a tsunami that typically follows after an earthquake. How long after the earthquake the wind turbine is extra sensitive to a horizontal load depends on the permeability of the enclosing soil, so the excess pore pressure can equalize with its surroundings. The change in soil stiffness also influences the eigenfrequency of the pile, as less of the soil damps the vibrations from waves and wind. As a rough simplification if the top 2 m is given a complete stiffness of zero the pile length above seabed is now 2 m longer reducing the eigenfrequency of the wind turbine.

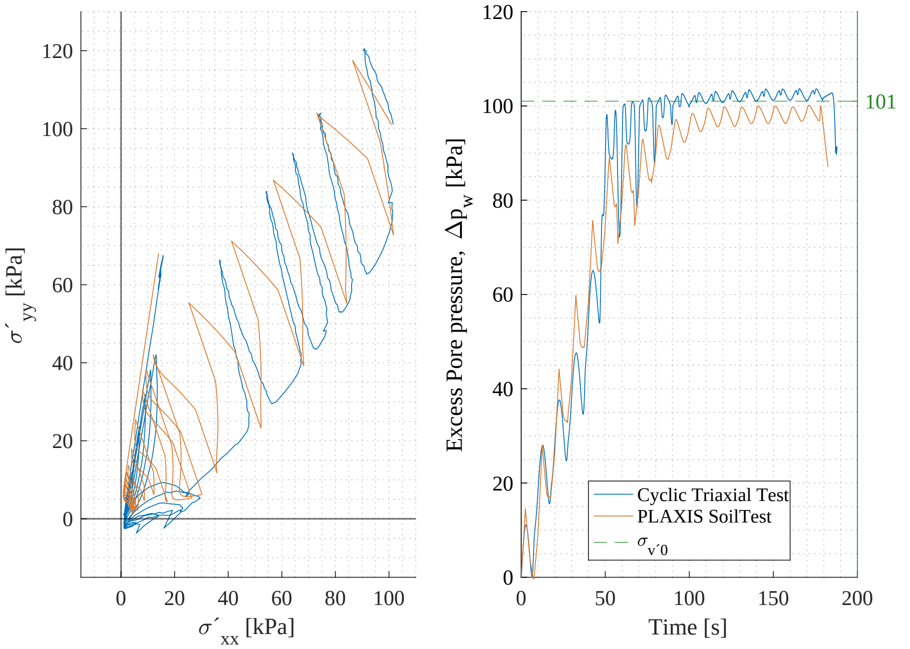

Figure 7.1: *Comparison between the cyclic triaxial test and the soil test in PLAXIS3D.*

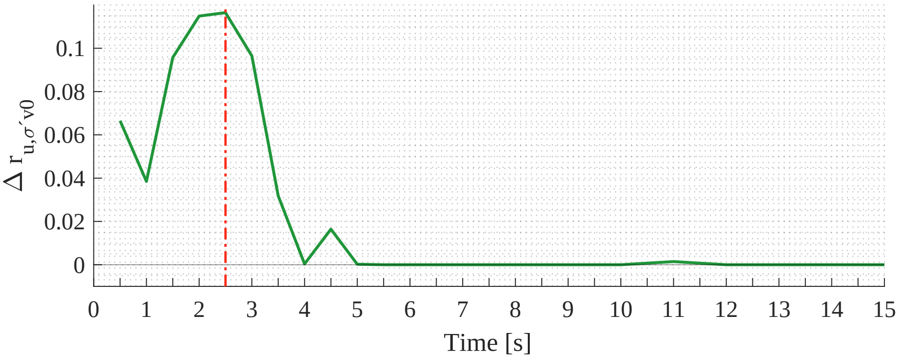

Figure 7.2: *Rate at which $r_{u,\sigma'v0}$ develops during the earthquake around the pile in a depth* 2 m.

7.1.3 Post-liquefaction soil pressure

In an effort to quantify the residual shear strength after the earthquake and with the top layer in a liquefied state a static analysis is conducted after the dynamic calculation. In this analysis the whole pile is displaced laterally a distance of 1.5 m and the resulting soil pressure on the pile is calculated. The soil pressure p on the pile as it moves through the soil, is directly related to the mobilized shear strength in the displaced soil *y*, c.f. Reese et al. (2002), and so the soil pressure-displacement relation is closely linked to the shear stress-shear strain relation.

From the multistage cyclic triaxial test the post-liquefaction shear stress-shear strain relation is shown in Figure 7.3. Here the initial shear modulus G_1 is very small compared to the shear modulus G_2 at large shear strains, and so for the soil to mobilize enough soil resistance on the pile sizable shear strains have to been reached.

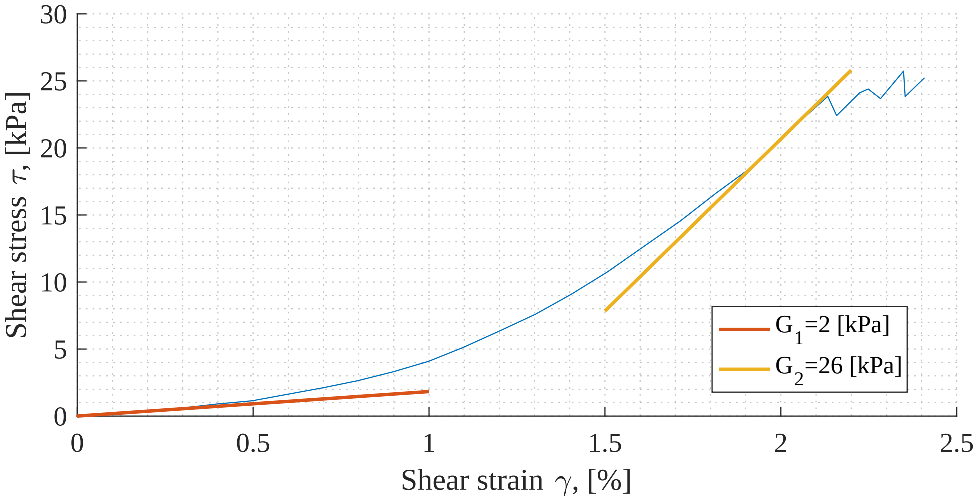

Figure 7.3: *Post-liquefaction shear stress-shear strain relation from multistage cyclic triaxial test. G_1 is the initial shear modulus and G_2 is the shear modulus after the soil have dilated.*

As the first two meters in the top layer is in a liquefied state the shear stress-shear strain relation here must resemble that of Figure 7.3. From PLAXIS Output the shear stresses and shear strains at XYZ-coordinates (4.5, 0, -0.2) are plotted in Figure 7.4.

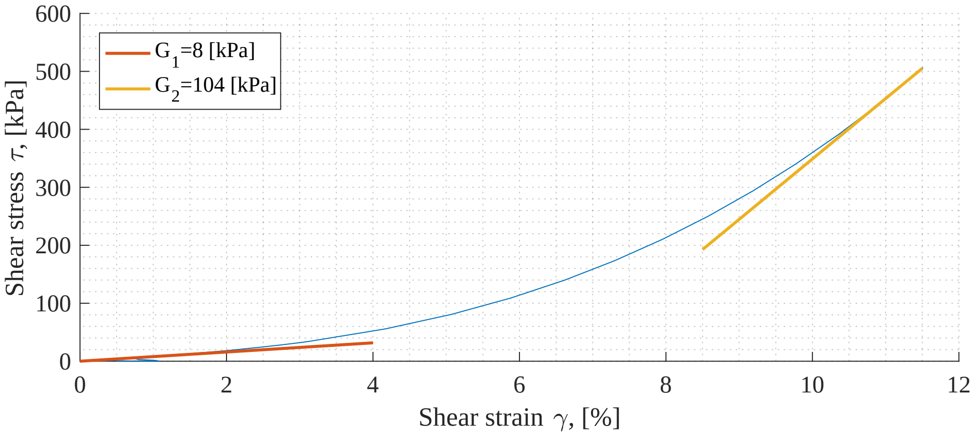

Figure 7.4: *Post-liquefaction shear stress-shear strain relation from PLAXIS at XYZ-coordinates (4.5, 0, -0.2) . G_1 is the initial shear modulus and G_2 is the shear modulus after the soil have dilated.*

The resemblance between the two shear stress-shear strain relations is immediately noticed just by the look of the shape of the blue curves. Although the scale of the axes is not the same the ratio between G_1 and G_2 is the same in the two plots ;

$$\frac{26}{2} = 13 \qquad \text{Laboratory test} \tag{7.1}$$

$$\frac{104}{8} = 13 \qquad \text{PLAXIS Output} \tag{7.2}$$

A clear definition of G_1 and G_2 is not determined, so the above ratio is sensitive to changes. However, the general trend of the stress-strain relation is captured in the PLAXIS Output.

The generated p-y relation is, as mentioned previously, associated with the shear stress-shear strain relation and must therefore coincide with the curve in Figure 7.4. In Figure 7.5 the p-y curve at $z = -1\,\mathrm{m}$ is shown with the dark dotted line as the secant line from origo to the end displacement at $y = 1.5\,\mathrm{m}$.

A comparison between Figure 7.4 and Figure 7.5 is a bit more difficult since the variables have changed from stresses and strains to pressure and displacement, respectively. However, the same trend can be spotted in the generated p-y curve with a ratio between the two tangent stiffness of

$$\frac{35060}{2327} = 15 \tag{7.3}$$

which is close to the ratio of 13 in Eq. (7.2).

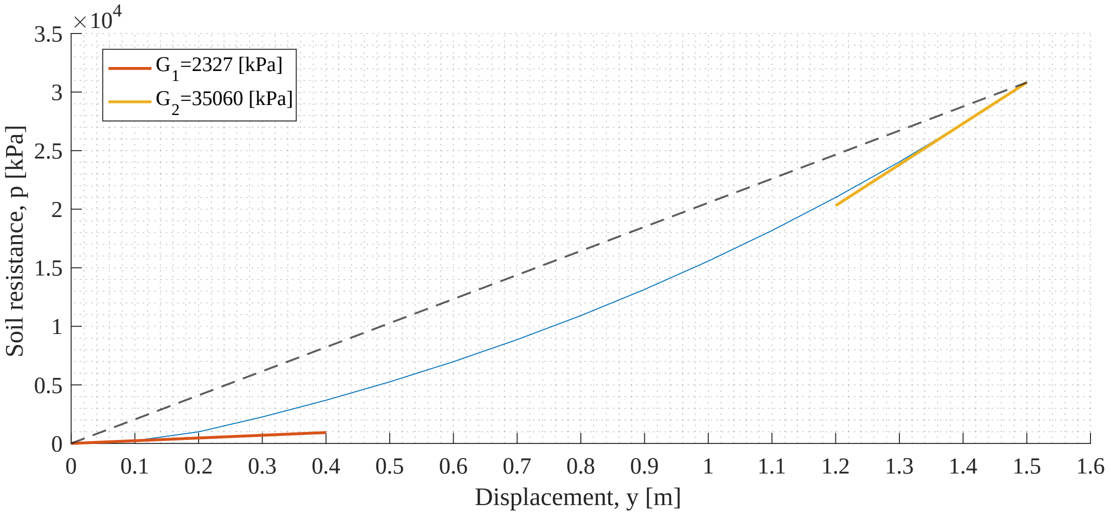

Figure 7.5: *P-y curve at* $z = -1\,\mathrm{m}$ *for the post-liquefied soil. The dotted dark line is the secant line from origin to* $y = 1.5\,\mathrm{m}$

Overall, the general trend of soil hardening is clearly traced through Figures 7.3 to 7.5 with an indication of stiffness ratio of $13-15$ between the stiffness at large strains/displacement and initial stiffness in post-liquefied soil. Further analyses could include a more detailed static calculation with a different soil model design

7.2 Conclusion

The stiffness parameters in the soil model UBC3D-PLM is calibrated using multistage triaxial test. The comparison shows good agreement in the generation of excess pore pressure and degradation in the stress path. A case investigated with the modelling of a monopile situated liquefiable soil shows how the pile displaces during an earthquake and how the excess pore pressure ratio increases in the first few seconds of the earthquake load, but ceases when the dynamic load terminate.

Generated p-y curves in the liquefied top soil show good resemblance with the post-liquefied shear stress-shear strain relation with a lateral displacement of $u = 1.5\,\mathrm{m}$.

Bibliography

Ashford, S. A., R. W. Boulanger, and S. J. Brandenburg
2011. Recommended design practice for pile foundations in laterally spreading ground. Technical report, Oregon State University.

Bao, X., Z. Xia, G. Ye, Y. Fu, and D. Su
2017. Numerical analysis on the seismic behavior of a large metro subway tunnel in liquefiable ground. *Tunnelling and Underground Space Technology*, 66:91–106.

Beaty, M. H. and P. M. Byrne
2001. Ubcsand constitutive model - version 904ar. Technical report, Itasca Web Site.

Brinkgreve, R.
2013. *Validating Numerical Modelling in Geotechnical Engineering*. NAFEMS.

Butterfield, K. and R. Davis
2004. Initiation of pore pressure rise in earthquakes. In *Cyclic Behaviour of Soils and Liquefaction Phenomena*, Pp. 289–293. Taylor & Francis.

Byrne, P. M., H. Puebla, D. H. Chan, A. Soroush, N. R. Morgenstern, D. C. Cathro, W. H. Gu, R. Phillips, P. K. Robertson, B. A. Hofmann, C. E. F. Wride, D. C. Sego, H. D. Plewes, B. R. List, and S. Tan
2000. CANLEX full-scale experiment and modelling. *Canadian Geotechnical Journal*, 37(3):543–562.

Chang, B. J. and T. C. Hutchinson
2013. Experimental evaluation of p-y curves considering development of liquefaction. *Journal of Geotechnical and Geoenvironmental Engineering*, 139(4):577–586.

COP21
2015. Paris agreement. Technical report, United Nations Framework Convention on Climate Change (UNFCCC).

Daftari, A. and W. Kudla
2014. Prediction of soil liquefaction by using ubc3d-plm model in plaxis. *International Journal of Environmental, Chemical, Ecological, Geological and Geophysical Engineering*, 8(2):106 – 111.

Daoud, S., I. Said, S. Ennour, and M. Bouassida
2018. Numerical analysis of cargo liquefaction mechanism under the swell motion. *Marine Structures*, 57:52–71.

Dash, S., M. Rouholamin, D. Lombardi, and S. Bhattacharya
2017. A practical method for construction of p-y curves for liquefiable soils. *Soil Dynamics and Earthquake Engineering*, 97:478–481.

DNV
2007. *DNV-OS-J101 October 2007. Design of Offshore Wind Turbines*, DNV Offshore Standard. Det Norske Veritas.

Ghorbani, A. A. . M. S. K.
2017. Numerical simulation of piles subjected to lateral spreading and comparison with shaking table results. *Civil Engineering Infrastructure Journal*, 50(2):277–292.

Janalizadeh, A. and A. Zahmatkesh
2015. Lateral response of pile foundations in liquefiable soils. *Journal of Rock Mechanics and Geotechnical Engineering*, 7(5):532–539.

Jefferies, M. and K. Been
2015. *Soil Liquefaction: A Critical State Approach, Second Edition (Applied Geotechnics)*. CRC Press.

Kallehave, D., B. W. Byrne, C. L. Thilsted, and K. K. Mikkelsen
2015. Optimization of monopiles for offshore wind turbines. *Philosophical Transactions of the Royal Society A: Mathematical, Physical and Engineering Sciences*, 373(2035):20140100–20140100.

Knudsen, B. S., M. U. Østergaards, L. B. Ibsen, and J. C. Clausen
2013. Determination of p-y curves for bucket foundations in sand using finite element modeling. Technical report, Department of Civil Engineering, Aalborg University.

Kramer, S.
1996. *Geotechnical Earthquake Engineering*. Prentice Hall.

Lombardi, D., S. Bhattacharya, M. Hyodo, and T. Kaneko
2014. Undrained behaviour of two silica sands and practical implications for modelling SSI in liquefiable soils. *Soil Dynamics and Earthquake Engineering*, 66:293–304.

Lombardi, D., S. R. Dash, S. Bhattacharya, E. Ibraim, D. M. Wood, and C. A. Taylor
2017. Construction of simplified design p–y curves for liquefied soils. *Géotechnique*, 67(3):216–227.

Luque, R. and J. D. Bray
2017. Dynamic analyses of two buildings founded on liquefiable soils during the canterbury earthquake sequence. *Journal of Geotechnical and Geoenvironmental Engineering*, 143(9):04017067.

Petalas, A. and V. Galavi
2013. Plaxis liquefaction model ubc3d-plm. Technical report, PLAXIS.

R.B.J Brinkgreve, e. a.
2017. *PLAXIS3D - Manuals*. Plaxis bv.

Reese, L., W. V. Impe, and R. Holtz
2002. Single piles and pile groups under lateral loading. *Applied Mechanics Reviews*, 55(1):B9.

Rouholamin, M., S. Bhattacharya, and R. P. Orense
2017. Effect of initial relative density on the post-liquefaction behaviour of sand. *Soil Dynamics and Earthquake Engineering*, 97:25–36.

Sivathayalan, S. and A. M. Yazdi
2004. Post liquefaction response of initially strain softening sand. In *Cyclic Behaviour of Soils and Liquefaction Phenomena*, Pp. 215–221. Taylor & Francis.

Tsegaye, A. B.
2010. Liquefaction model. Technical Report No. 1, Plaxis B.V.

Wobbes, E., L. Beuth, C. Vuik, and D. Stolle
2017. Modeling of liquefaction using two-phase FEM with UBC3d-PLM model. *Procedia Engineering*, 175:349–356.

Wolf, T. K., K. L. Rasmusenn, M. Hansen, H. R. Roesen, and L. B. Ibsen
2013. Assessment of p-y curves from numerical methods for a non-slender monopile in cohesionless soil. Technical report, Department of Civil Engineering, Aalborg University.

Appendix A

Excess Pore Pressure Ratio

The excess pore pressure ratio for every string can be seen from Figures A.1 to A.4.

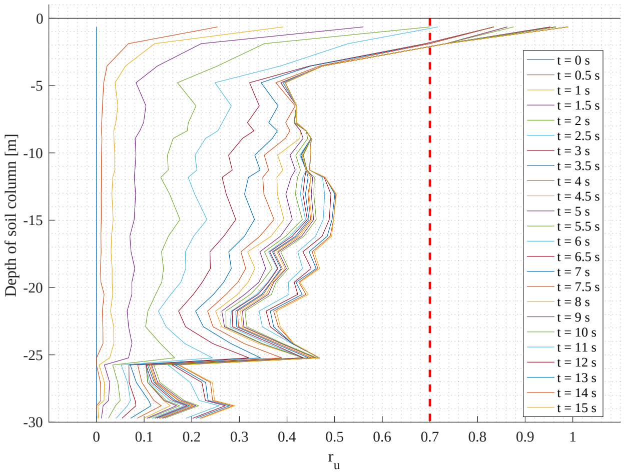

Figure A.1: *Excess pore pressure ration r_u at string number 1.*

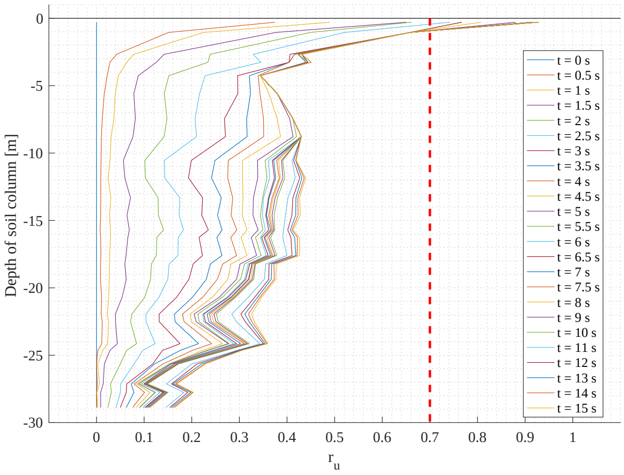

Figure A.2: *Excess pore pressure ration r_u at string number 2.*

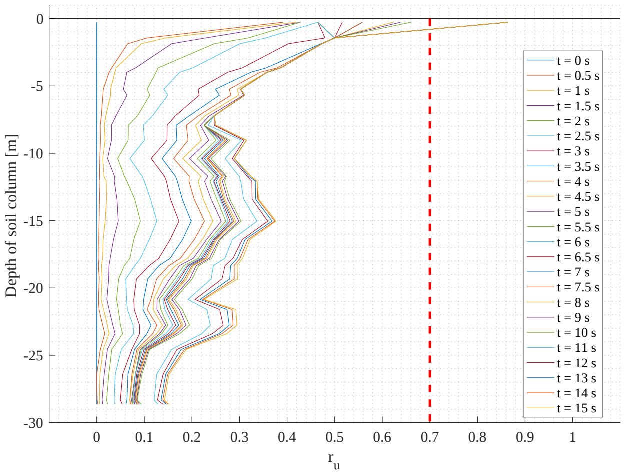

Figure A.3: *Excess pore pressure ration r_u at string number 3.*

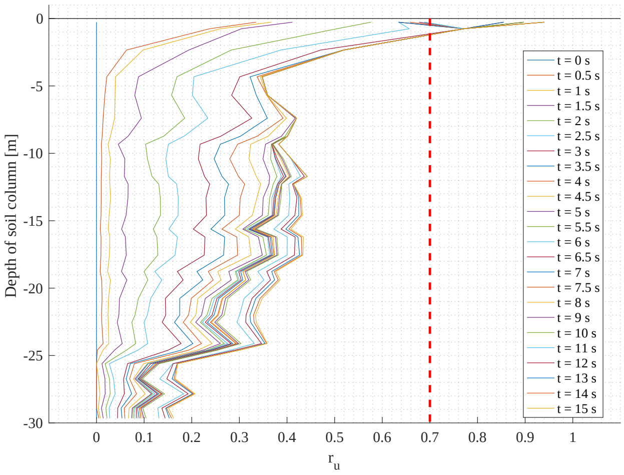

Figure A.4: *Excess pore pressure ration r_u at string number 4*

The excess pore pressure ratio at different time step durin the dynamic calculation can be seen from Figures A.5 to A.9.

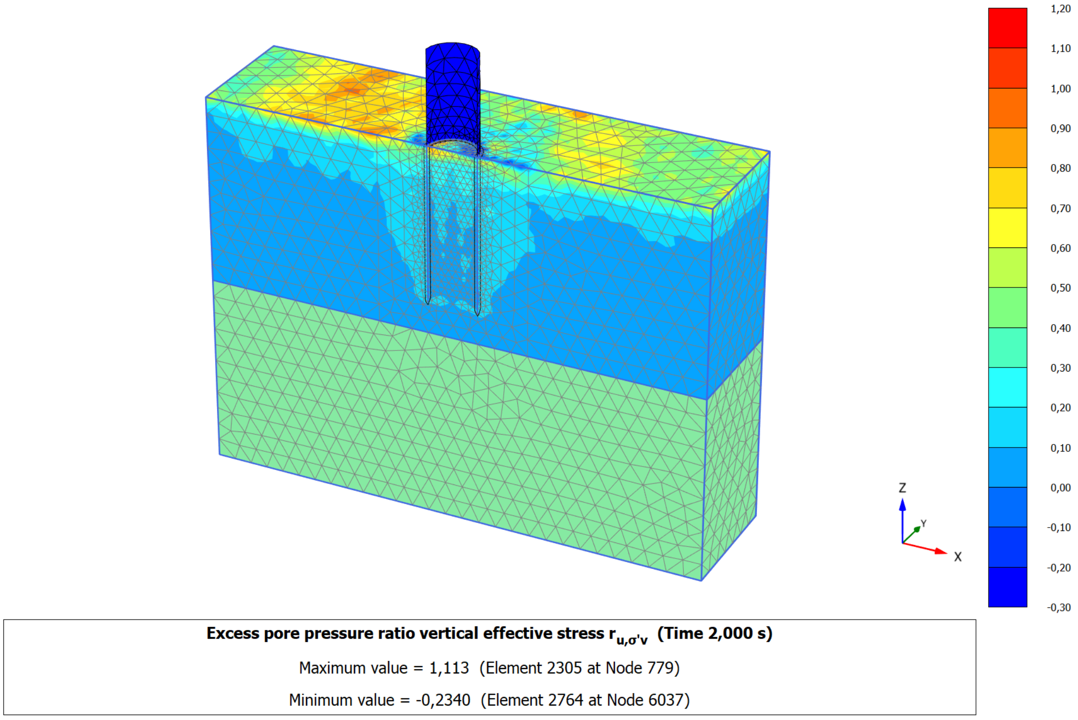
1,20
1,10
1,00
0,90
0,80
0,70
0,60
0,50
0,40
0,30
0,20
0,10
0,00
-0,10
-0,20
-0,30
Z
Y
X

Excess pore pressure ratio vertical effective stress $r_{u,\sigma'v}$ (Time 2,000 s)

Maximum value = 1,113 (Element 2305 at Node 779)

Minimum value = -0,2340 (Element 2764 at Node 6037)

Figure A.5: *Screen shot of* $r_{u,\sigma' v0}$

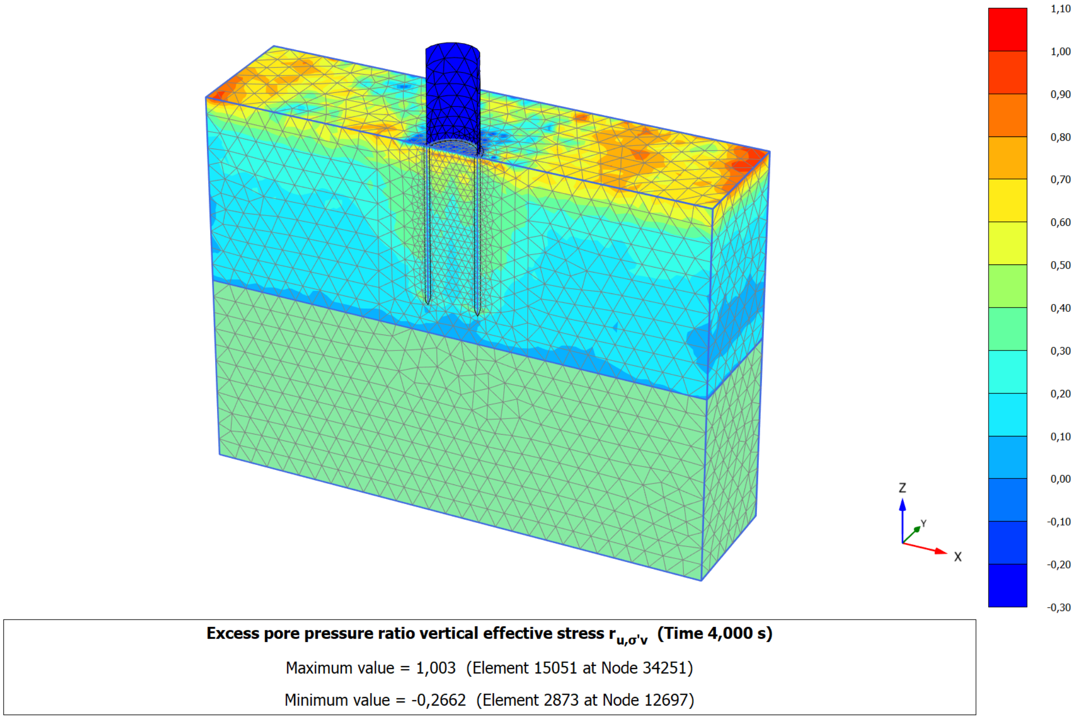
1,10
1,00
0,90
0,80
0,70
0,60
0,50
0,40
0,30
0,20
0,10
0,00
-0,10
-0,20
-0,30
Z
Y
X

Excess pore pressure ratio vertical effective stress $r_{u,\sigma'v}$ (Time 4,000 s)

Maximum value = 1,003 (Element 15051 at Node 34251)

Minimum value = -0,2662 (Element 2873 at Node 12697)

Figure A.6: *Screen shot of* $r_{u,\sigma' v0}$

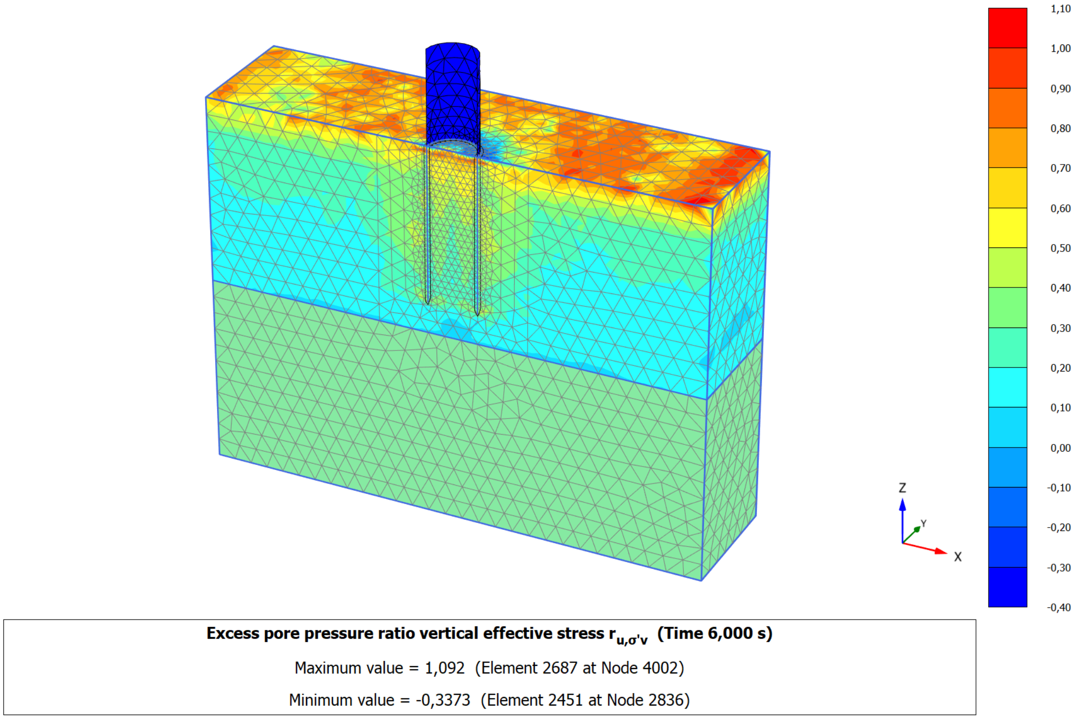
1,10
1,00
0,90
0,80
0,70
0,60
0,50
0,40
0,30
0,20
0,10
0,00
-0,10
-0,20
-0,30
-0,40
Z
Y
X

Excess pore pressure ratio vertical effective stress $r_{u,\sigma'v}$ (Time 6,000 s)

Maximum value = 1,092 (Element 2687 at Node 4002)

Minimum value = -0,3373 (Element 2451 at Node 2836)

Figure A.7: *Screen shot of* $r_{u,\sigma' v0}$

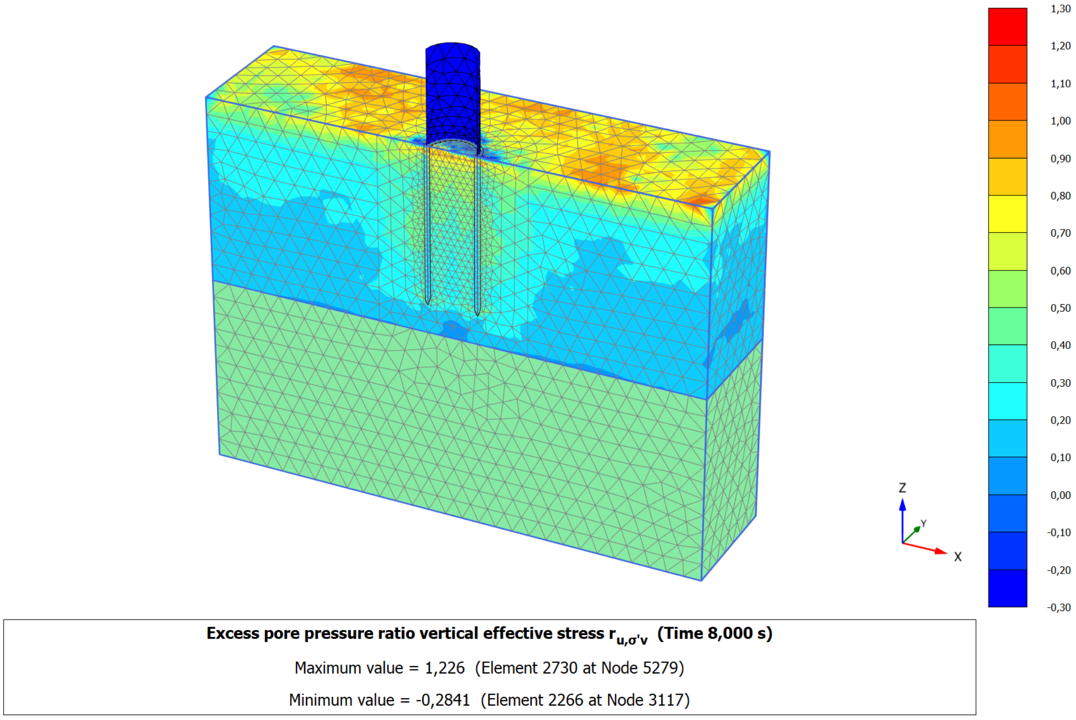
1,30
1,20
1,10
1,00
0,90
0,80
0,70
0,60
0,50
0,40
0,30
0,20
0,10
0,00
-0,10
-0,20
-0,30
Z
Y
X

Excess pore pressure ratio vertical effective stress $r_{u,\sigma'v}$ (Time 8,000 s)

Maximum value = 1,226 (Element 2730 at Node 5279)

Minimum value = -0,2841 (Element 2266 at Node 3117)

Figure A.8: *Screen shot of* $r_{u,\sigma' v0}$

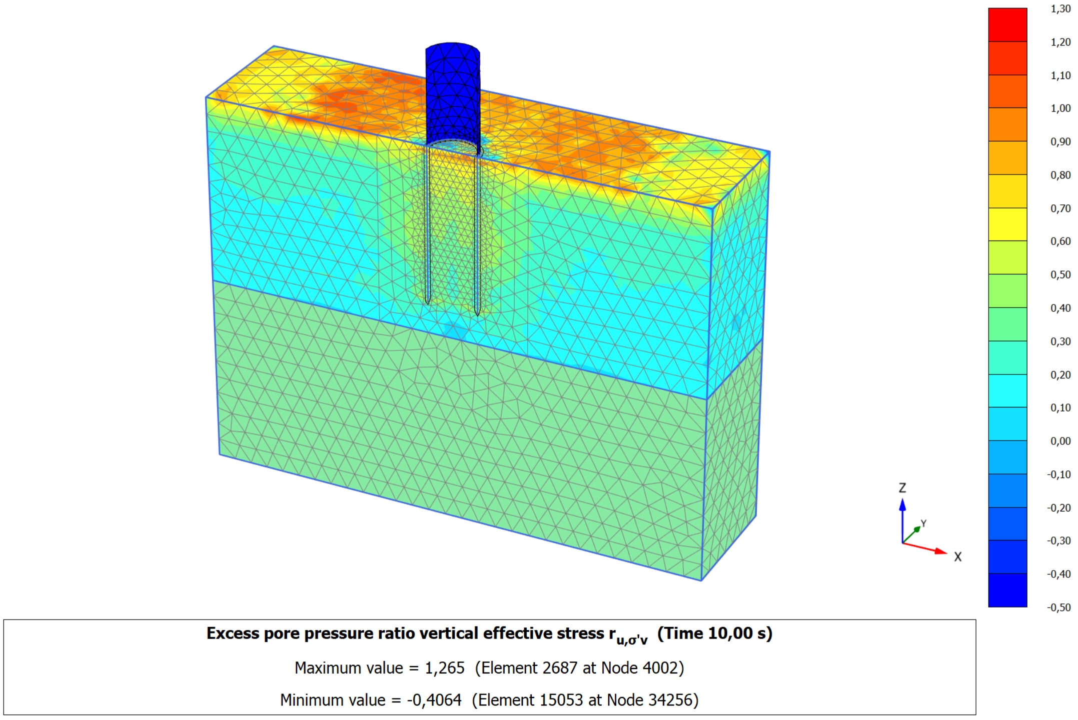
1,30
1,20
1,10
1,00
0,90
0,80
0,70
0,60
0,50
0,40
0,30
0,20
0,10
0,00
-0,10
-0,20
-0,30
-0,40
-0,50
Z
Y
X

Excess pore pressure ratio vertical effective stress $r_{u,\sigma'v}$ (Time 10,00 s)

Maximum value = 1,265 (Element 2687 at Node 4002)

Minimum value = -0,4064 (Element 15053 at Node 34256)

Figure A.9: *Screen shot of* $r_{u,\sigma' v0}$

Appendix B

Verification of code to establish p-y relation

The verification of code to determine the relation between the pile displacement and the soil resistance is done with a simple lateral displacement for drained soil using a Mohr-Coloumb constitutive relation.

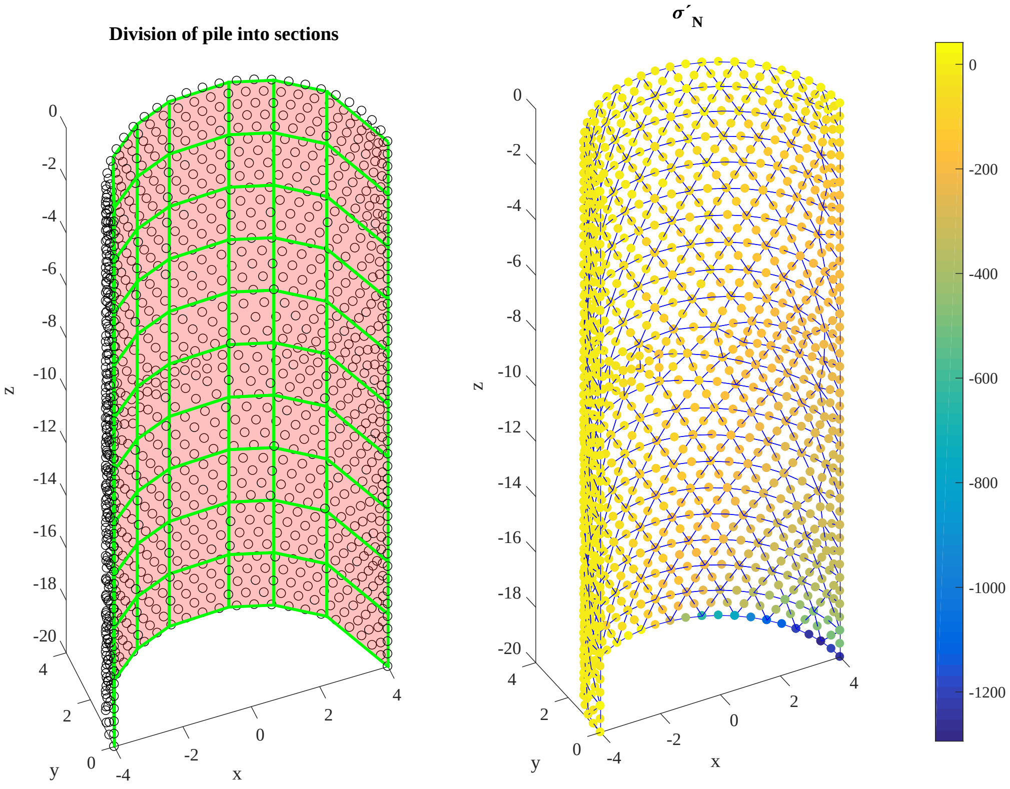

Figure B.1: *Section division for the reference calculation together with the normal stress acting on the circumference of the pile. The pile is divided into 70 sections.*

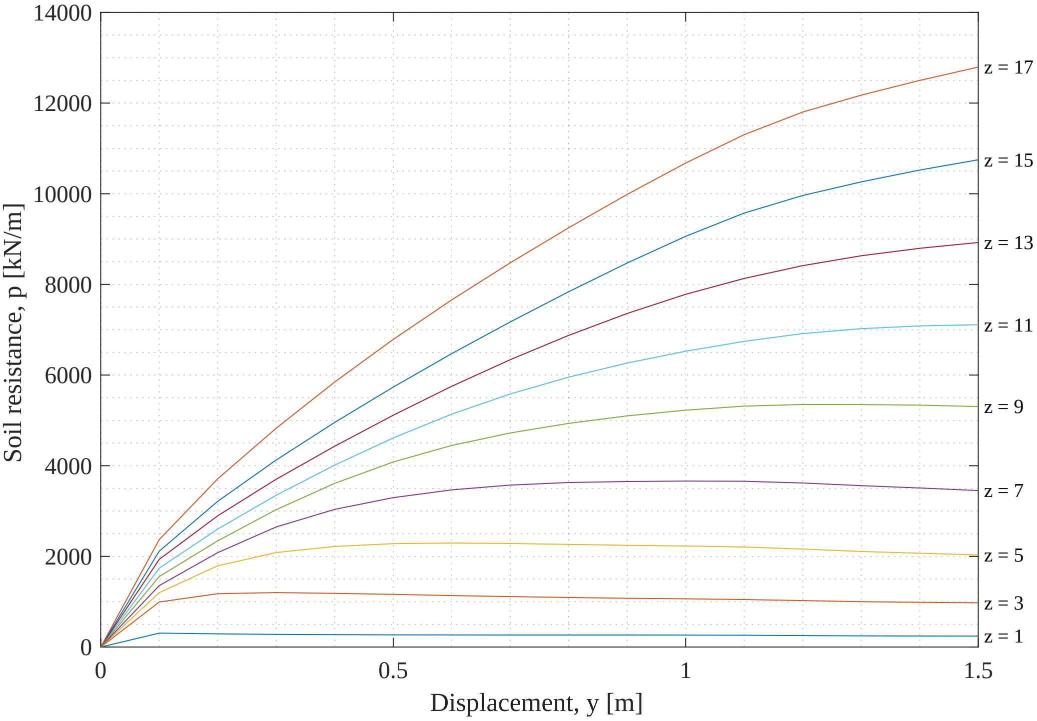

Figure B.2: *P-y curves for normal drained sand calculated with a Mohr-Columb constitutive relation.*